Reaction-induced mantle weakening at HP conditions: an example from garnet pyroxenites of Ulten zone (Eastern Alps, N Italy)

L. Pellegrino[1], L. Menegon[2,3], S. Zanchetta[1], F. Langenhorst[4,5], K. Pollok[4], S. Tumiati[6], N. Malaspina[1]

[1]Department of Earth and Environmental Sciences, University of Milano Bicocca, Piazza della Scienza 4, 20126, Milano, Italy

[2]The Njord Centre, Department of Geosciences, University of Oslo, Postbox 1048, Blindern, 0316 Oslo, Norway

[3]School of Geography, Earth and Environmental Sciences, University of Plymouth, Drake Circus, PL48AA Plymouth, UK

[4]Institute of Geosciences, Friedrich Schiller University Jena, Carl-Zeiss-Promenade 10, 07745 Jena, Germany

[5]Hawai'i Institute of Geophysics and Planetology, School of Ocean and Earth Science and Technology, University of Hawai'i at Manoa, Honolulu, HI 96822, USA

[6]Department of Earth Sciences, University of Milano, via Mangiagalli 34, 20133 Milano, Italy

Corresponding author: Luca Pellegrino (luca.pellegrino@unimib.it)

Key Points:

- In websterites of Ulten zone, pyroxenes switch from dislocation to diffusion creep dominated deformation.
- The transition in deformation mechanism took place during the prograde re-equilibration of websterites in the garnet stability field.
- This results in the rheological weakening of websterites during the corner flow of the lithospheric mantle induced by the slab subduction.

Abstract

Peridotites of Ulten Zone (Eastern Alps, N Italy) show a transition from coarse protogranular spinel lherzolites to finer-grained amphibole + garnet peridotites, recorded by the crystallization of garnet coronas around spinel. Pyroxenite veins, transposed along the peridotite foliation, show a similar metamorphic evolution from coarse-grained (garnet-free) websterites to finer-grained garnet websterites. In both peridotites and websterites, garnet previously exsolved from porphyroclastic high-temperature pyroxenes and later crystallized along the foliation. This evolution has been interpreted to reflect cooling and pressure increase of both websterites and host peridotites from spinel- to garnet-facies conditions.

Microstructures and crystallographic orientation data indicate that the re-equilibration of garnet websterites in the garnet stability field occurred in a deformation regime. Pyroxene porphyroclasts show a crystallographic preferred orientation which is consistent with dislocation creep on the (100)[010] slip system. Core-and-mantle microstructures also suggest that dislocation creep was aided by subgrain rotation recrystallization, leading the formation of neoblastic pyroxene grains. These recrystallized grains dominantly deform by diffusion-accommodated grain boundary sliding, as indicated by the occurrence of four grain junctions and straight, aligned grain boundaries.

The transition from dislocation creep to diffusion creep was also accompanied by the crystallization of garnet along the garnet websterite foliation, which triggered the pinning of the recrystallized matrix and stabilized the fine-grained microtexture for diffusion creep, facilitating the rheological weakening of garnet websterites.

Garnet websterites of Ulten Zone thus offer a unique opportunity to investigate the effects of reaction softening during the corner flow of the lithospheric mantle induced by the slab subduction.

Plain Language Summary

When tectonic plates converge, one plate slides beneath the other plate descending into the Earth's mantle. During this process (the so-called subduction) rocks forming the Earth's mantle, such as peridotites and pyroxenites, can be dragged to great depths and later transported back to the surface by a combination of two processes known as corner flow and exhumation. Rocks that experienced this journey are now exposed at the surface only in few mountain belts in the world (such as the European Alps) and represent natural laboratories to study the processes that occur at great depths in the Earth's mantle.

In this study we reconstruct the metamorphic and deformation evolution of pyroxenites of the Ulten Zone (Eastern Alps, N Italy). Minerals in pyroxenites deformed through different deformation processes, including dislocation creep and diffusion creep mechanisms. Our data indicate that minerals within pyroxenites record a transition in the deformation mechanism from dislocation to diffusion creep. This switch of the deformation mechanism was responsible for a significant rheological weakening of pyroxenites, suggesting that pyroxenites can play a major role in the processes that control the deformational behavior of the Earth's mantle.

1 Introduction

The deformational behavior of the upper mantle in response to the forces in the Earth's interior depends on several factors, including pressure, temperature, deviatoric stress, mineralogy,

presence of fluids and/or melts, and the grain size of the deforming mantle rocks (e.g. Bürgmann & Dresen, 2008 and reference therein). Studies on both naturally and experimentally deformed mantle rocks indicate that most of the plastic deformation of the upper mantle is accommodated by grain size insensitive (GSI) deformation mechanisms, e.g. dislocation creep (Bai and Kohlstedt, 1992; Demouchy et al., 2009; Doukhan et al., 1984; Durham and Goetze, 1977; Durham et al., 1977; Jung et al., 2006).

In particular, at upper mantle conditions, mantle minerals (e.g. olivine and pyroxenes) are expected to deform through dislocation glide and creep on specific crystallographic planes and directions (slip systems), resulting in the formation of a crystallographic preferred orientation (CPO), which is a function of the available slip systems and the strain regime. However, field-based microstructural studies on mantle shear zones suggest that a significant part of the deformation may be also accommodated by grain-size sensitive (GSS) creep processes, e.g. diffusion creep and grain boundary sliding (Warren & Hirth, 2006; Skemer et al., 2010; Kaczmarek & Tommasi, 2011; Vauchez et al., 2012). These studies also highlight that the grain size within shear zones is typically smaller than the grain size of the host rocks (e.g. Drury et al., 1991; White et al., 1980), suggesting that dynamic recrystallization co-operates with creep mechanisms during deformation and strain localization. Grain-size reduction by dynamic recrystallization is believed to be the principal responsible of the transition in the deformation mechanism from dislocation creep to diffusion creep processes (Handy, 1989; Jaroslow et al., 1996; Skemer et al., 2010; Toy et al., 2010), and thus of the consequent rheological weakening (Hansen et al., 2011; Hirth & Kohlstedt, 2003; Rutter & Brodie, 1988). However, De Bresser et al., (2001) demonstrated that grain size reduction may be not sufficient to cause a permanent transition from dislocation to diffusion creep because minerals tend to grow with time. Nevertheless, syn-deformational metamorphic reactions are able to inhibit grain growth (e.g. Newman et al., 1999), since the crystallization of new minerals (i.e. the so-called second phases) can trigger the pinning of the recrystallized matrix, preventing grain coarsening, and thus stabilizing the fine-grained microtexture for diffusion creep (Linckens et al., 2011; Précigout et al., 2007; Warren and Hirth, 2006).

Microstructural studies on natural rocks indicate that syn-deformational metamorphic reactions such as the breakdown of mantle aluminous phases (plagioclase, spinel or garnet) can promote rheological weakening in the upper mantle (e.g. Furusho & Kanagawa, 1999; Hidas et al., 2013; Kaczmarek & Tommasi, 2011; Newman et al., 1999; Toy et al., 2010). These studies demonstrate that syn-deformational breakdown reactions generate fine-grained reaction products in which deformation can be localized. This process triggers the transition from dislocation to diffusion creep, thus facilitating rheological weakening. Experimental studies also indicate that the transition from plagioclase to spinel and garnet facies in the mantle is strongly affected by the whole-rock concentration of major elements such as Al_2O_3, Cr_2O_3, CaO and Na_2O (Adam et al., 1992; Borghini et al., 2010; Fumagalli & Poli, 2005; Irving, 1974; Schmädicke, 2000; Ziberna et al., 2013). In particular, these studies pointed out that the breakdown of these aluminous minerals occurs at different pressure in pyroxene-rich mantle rocks compared to peridotites, therefore suggesting that the locus and the degree of deformation in the upper mantle may be also controlled by the occurrence and the distribution of compositional heterogeneities like pyroxenites l.s..

The Ulten zone (Tonale nappe, Eastern Alps, N Italy) is one of the best examples of metamorphic terrane where peridotites from the supra-subduction mantle record the transition

from spinel- to garnet-facies conditions resulting from the corner flow triggered by the subduction of an old continental crust (Godard et al. 1996; Nimis and Morten 2000; Scambelluri et al., 2010; Tumiati et al., 2003). These peridotites are veined by numerous websterites, which record the same textural/metamorphic evolution of the host rocks (Gebauer & Grünenfelder, 1978; Nimis & Morten 2000). We will show that these websterites underwent a textural transformation from coarse-grained (garnet-free) to finer-grained (garnet-bearing) websterites reflecting the cooling and pressure increase from spinel- to garnet-facies conditions during the mantle corner flow. In particular, microstructures indicate that the transition to garnet-facies conditions occurred in a deformation regime and was accompanied by a reaction-induced reduction of the grain size, which triggered the switch of the deformation mechanism from dislocation creep to diffusion creep. This process resulted in the rheological weakening of garnet websterites, which also affected the host peridotites.

2 Geological and petrological background

The Ulten zone (hereafter UZ) forms the northern part of the Tonale nappe, belonging to the Austroalpine tectonic domain of the Eastern Alps (Figure 1a). It represents a high-grade basement unit containing slivers of amphibolitized eclogites (Del Moro et al., 1999; Tumiati et al., 2003) and peridotites that reached peak metamorphic conditions during the late Paleozoic Variscan orogeny (Godard et al., 1996; Herzberg et al., 1977; Hoinkes & Thöni, 1993; Martin et al., 1993; Obata & Morten, 1987; Tumiati et al., 2003, 2007).

Mafic and ultramafic bodies are surrounded by mylonitic, garnet + kyanite stromatic gneisses and garnet + kyanite diatexites (Ranalli et al., 2005). The felsic migmatites and the amphibolitized eclogites record a complex evolution from eclogite-, to granulite-, to amphibolite-facies conditions. Maximum pressures and temperatures experienced by migmatitic felsic rocks have been calculated at 1.5-2.5 GPa and 700-850 °C (Braga et al., 2007; Godard et al. 1996; Hauzenberger et al., 1996; Hoinkes & Thöni 1993; Tumiati et al. 2003). Migmatization took place under fluid-absent conditions by phengite dehydration melting at temperatures of 850 °C and pressures of 1.5-2.5 GPa (Godard et al., 1996; Hauzenberger et al., 1996; Tumiati et al., 2003), and likely occurred either during prograde subduction or the early stages of exhumation after stromatic gneiss and diatexites reached the pressure peak (Tumiati et al., 2003).

In the field, peridotites occur as meters to hundreds of meters long lenses aligned along a discontinuous band at the transition between the stromatic gneisses and the diatexites (Figure 1a and 1b). Peridotites show a transition from coarse protogranular spinel lherzolites (coarse-type of Obata & Morten, 1987) to finer-grained amphibole + garnet peridotites (fine-type of Obata & Morten, 1987). Thermobarometric estimates on spinel-facies assemblages yielded equilibrium condition of P = 1.3-1.6 GPa and T = 1200 °C (Nimis & Morten, 2000). During this stage, peridotites were infiltrated by hydrous melts rising from the deep regions of the lithospheric mantle, precipitating coarse-grained websterites in the host peridotites (Nimis & Morten, 2000). These pyroxenites record a textural evolution similar to that of the host peridotites, and change from coarse-grained websterites (clinopyroxene + orthopyroxene ± olivine) to finer-grained garnet websterites. The re-equilibration of websterites and peridotites in the garnet stability field is calculated to have occurred at P = 2.0-2.7 GPa and T = 850 °C (Braga & Sapienza, 2007; Malaspina & Tumiati, 2012; Nimis & Morten, 2000; Tumiati et al., 2003). At these conditions, garnet formed at the expenses of spinel in peridotites, exsolved from porphyroclastic, high-T pyroxenes in both peridotites and websterites, and crystallized along the foliation of websterites

and host peridotites. This evolution has been interpreted to reflect cooling and pressure increase of websterites and host peridotites due to the mantle corner flow from hot regions of the subcontinental lithospheric mantle to deeper and cooler mantle domains located at the top of the slab (Nimis & Morten, 2000).

The re-equilibration at high pressure of websterites and hosting peridotites was accompanied by intense shearing and fluid infiltration (Obata & Morten, 1987; Rampone & Morten, 2001). Indeed, hydration related to the high pressure metamorphism promoted the formation of garnet + amphibole-bearing assemblages in both websterites and peridotites (Obata & Morten, 1987), and the crystallization of metasomatic minerals such as phlogopite, dolomite, allanite, and dissakisite-(La) in peridotites (Lavina et al., 2006; Malaspina & Tumiati, 2012; Marocchi et al., 2009; Morten & Trommsdorff, 2003; Sapienza et al., 2009; Susini & Martin, 1996; Tumiati et al., 2005), suggesting recrystallization under the influence of slab-derived fluids (Rampone & Morten 2001; Scambelluri et al, 2006; Tumiati et al. 2007).

Finally, the exhumation and re-equilibration at low pressure of the UZ peridotites is documented by spinel + orthopyroxene + clinopyroxene + amphibole and orthopyroxene + amphibole + clinopyroxene kelyphites around garnet and the complete replacement of garnet by chlorite pseudomorphs or by coarse-grained amphibole + spinel aggregates (Martin et al., 1998; Godard et al., 2000).

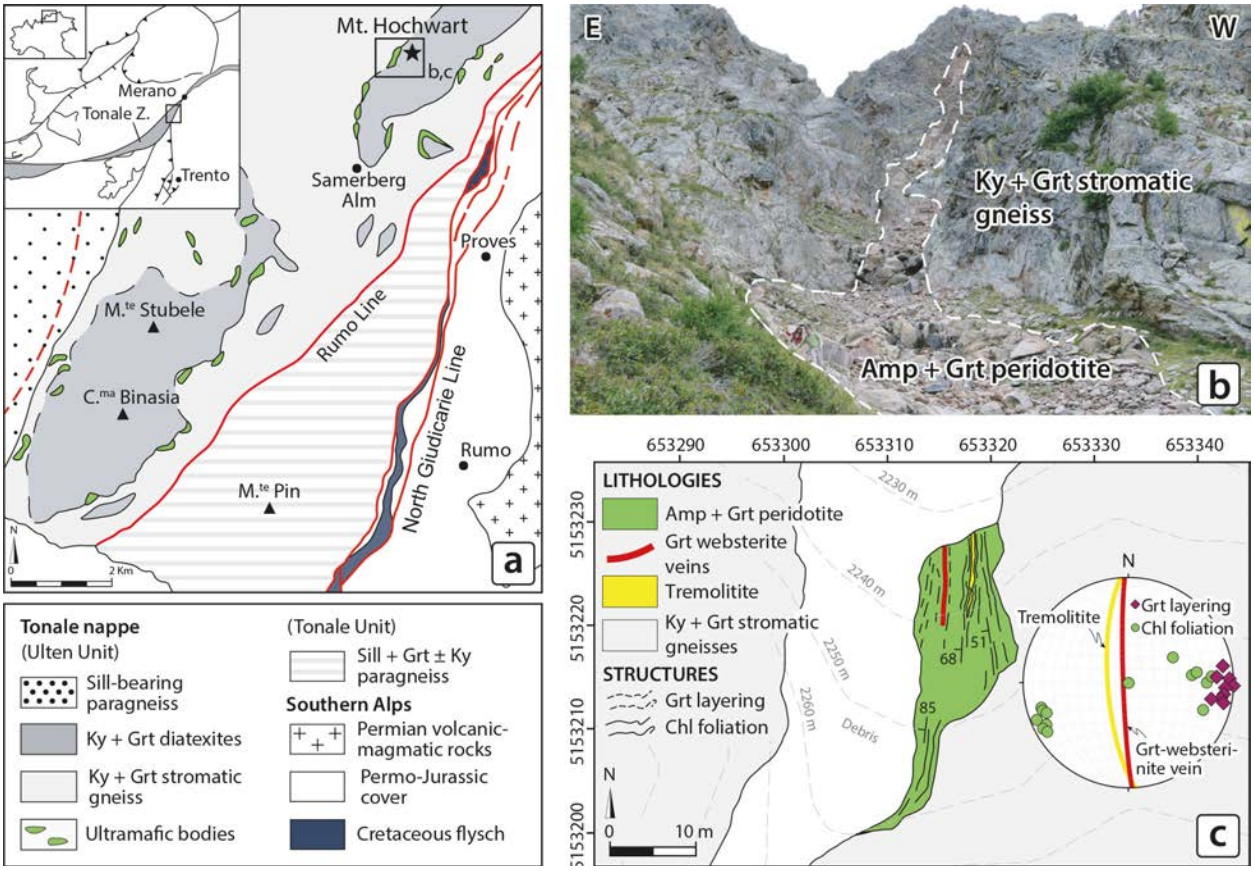

Figure 1. (a) Simplified geological map of Ulten Zone (UZ; Redrawn after Del Moro at al., 1999). The heavy rectangle is the framework for Figures 1b and 1c; (b) Mt. Hochwart amphibole

+ garnet peridotite body (N. Malaspina and S. Tumiati for scale); (c) detailed geological map of the Mt. Hochwart amphibole + garnet peridotite body.

3 Materials and Methods

Electron backscattered diffraction (EBSD) analyses on clinopyroxene and orthopyroxene in garnet websterites were carried out on a JEOL 6610 VP-SEM equipped with an Oxford Instruments Nordlys Nano EBSD detector and a JEOL 7001 FEG SEM equipped with a NordLys Max EBSD detector (AZTec acquisition software, Oxford Instruments) at the Electron Microscope Centre of the University of Plymouth, and a Zeiss Gemini 500 FEG SEM equipped with a e-Flash EBSD detector (Quantax EBSD acquisition software, Bruker) at the University of Milono Bicocca. EBSD patterns were acquired on rectangular grids with step sizes of 0.14, 1.3, 2.0 and 2.8 µm. Working conditions were 20 kV accelerating voltage, 10 nA of beam current, high vacuum, 70° sample tilt, and working distance between 17 and 23 mm. A detailed description of the EBSD sample preparation and post-processing methods is reported in the supporting information (Text S1). For grain size measurements, grain boundaries were manually traced on backscattered electron (BSE) and secondary electron (SE) images, or derived from crystallographic orientation data acquired by EBSD analyses. In this latter case, grain boundaries were defined for critical misorientations of 10°, while for subgrain size analysis were considered only closed subgrain boundaries defined for critical misorientation angles of 2°. The grain size and the subgrain size were measured using the mean linear intercept method following the American Society for Testing and Materials ASTM El12-12 procedure. Test lines were traced parallel, normal and randomly-oriented with respect to the foliation. A stereological correction factor of 1.5 was applied. Results are listed in Table S1.

Transmission electron microscopy (TEM) investigations were performed at the Friedrich Schiller University Jena. For TEM characterization, we prepared thin sections with an acetone soluble glue. Copper grids were mounted with two-component resin on the free surface of thin sections at sites of interest. These grids including the interesting areas were removed from slides by acetone dissolution. The sample grids were then Ar ion-thinned in a Gatan Duomill ion milling machine at 4.5kV and 1mA until electron transparency was reached. TEM characterization of defect microstructures was carried out with a 200 kV FEI Tecnai G2 F20 TEM, using conventional bright-field and dark-field imaging techniques in combination with selected area electron diffraction (SAED). To search larger areas for lattice defects we have also used the high-angle annular dark-field (HAADF) detector at low magnification scanning transmission electron microscopy (LM-STEM) mode with a very long camera length to obtain diffraction contrast images. The mineral identification was aided by energy-dispersive X-ray (EDX) spectra using an Oxford X-MaxN 80T SDD system.

Thermodynamic modelling was performed with the software package Perple_X (Connolly, 2005), using the thermodynamic database of Holland and Powell (1998) revised in 2002 (hp02ver.dat), and the following solution models described by Holland and Powell (1998) (HP), Holland and Powell (2003) (I1, HP and C1) and Dale et al. (2000) (D): Gt(HP) for garnet, Opx(HP) for orthopyroxene, O(HP) for olivine, Omph(HP) for Ca-Na clinopyroxene, Sp(HP) for spinel, Ca-Amp(D) for calcic amphibole, Chl(HP) for chlorite, Pl(I1, HP) for ternary feldspars. The water equation of state was taken from Holland and Powell (1998).

4 Results

4.1 Field Observations

In the northern sectors of the UZ, amphibole + garnet peridotite lenses and country stromatic gneisses are well-exposed along a steep gully on the western ridge of the Mt. Hochwart (Figure 1a and b). The peridotite body is continuous from the base of the gully (2233 m) up to the Hochwart Pass (2475 m). Amphibole + garnet peridotites (green in Figure 1c) have a porphyroclastic texture with coarse (up to 1-2 cm) amphibole and garnet porphyroclasts (reaching up to 9 cm in diameter in the inner part of the peridotite body) embedded in a finer-grained matrix consisting of olivine, orthopyroxene, amphibole and rare clinopyroxene. Garnets are invariably mantled by spinel + orthopyroxene + clinopyroxene ± amphibole kelyphitic coronas or replaced by chlorite pseudomorphs. Peridotites display a steep W-dipping compositional layering consisting of garnet-rich and garnet-poor bands locally transposed by a chlorite foliation that becomes more penetrative at the contact with the surrounding stromatic gneisses (Figure 2a). Peridotites include centimeter-thick garnet websterite veins (red in Figure 1c; Figure 2b) which occur parallel to the garnet foliation in the peridotite. They are characterized by clinopyroxene and orthopyroxene porphyroclasts (up to 5 mm) enclosed in a finer-grained matrix composed by emerald-green Cr-diopside, orthopyroxene, amphibole and garnet. The anisotropic fabric of the garnet websterites is marked by garnet-rich and garnet-poor levels that dip to the west parallel to the garnet layering in the host peridotite. Peridotites also contain meter-scale tremolitite layers (yellow in Figure 1c) consisting of tremolite (80-90 vol%) with subordinate chlorite pseudomorphs after garnet and minor Mg-hornblende. Tremolitites are strongly stretched and boudinaged parallel to chlorite foliation in the peridotite.

The contact between peridotites and country stromatic gneisses is often marked by metasomatic reaction zones with a composite structure consisting of an inner tremolite-rich cm-thick layer on the peridotite side and an outer phlogopite-rich front toward the host gneiss (see also Marocchi et al., 2009, 2010; Tumiati & Martin, 2003; Tumiati et al., 2007).

The country gneisses (light grey in Figure 1c) have a stromatic texture characterized by cm-spaced bands of quartz + plagioclase + K-feldspar ± garnet ± kyanite leucosomes and garnet + kyanite + biotite melanosomes (restites) transposed along the regional foliation (for a detailed description of these rocks see also Del Moro et al., 1999; Martin et al., 1998; Tumiati et al., 2003).

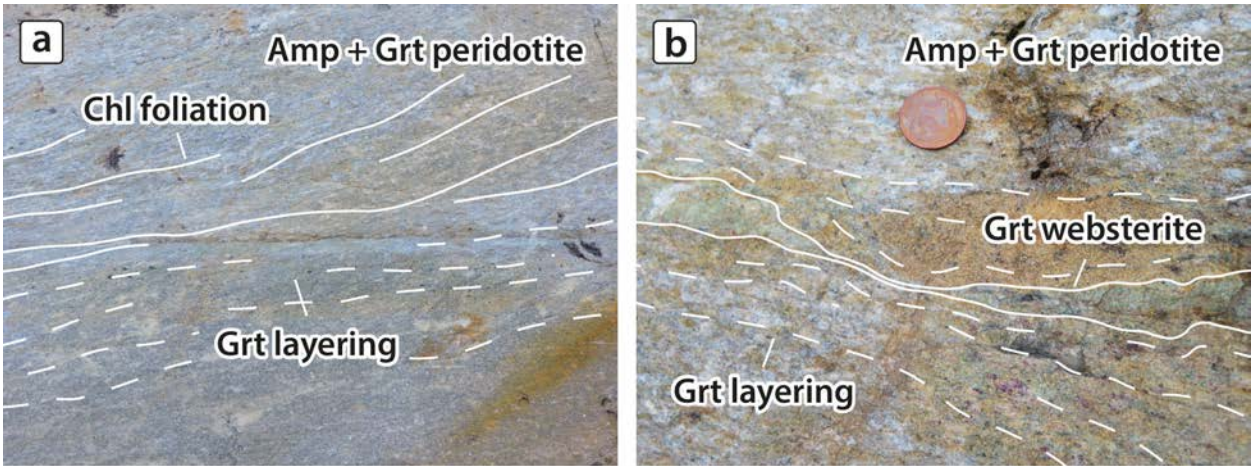

Figure 2. Structures of amphibole + garnet peridotites and garnet websterites of UZ. (a) Garnet layering transposed by a chlorite foliation in amphibole + garnet peridotites; (b) Garnet websterite vein transposed along the garnet layering of amphibole + garnet peridotites.

4.2 Microstructures

Representative samples of garnet websterites have been selected for this study. Sample location and coordinates are given in Figure S1 of supporting information. Mineral abbreviations are from Whitney and Evans (2010).

4.2.-1 Garnet websterites

Garnet websterites have a porphyroclastic texture with coarse (up to 3 mm) orthopyroxene (Opx_P) and clinopyroxene (Cpx_P) porphyroclasts surrounded by finer-grained, dynamically recrystallized, neoblastic clinopyroxene (Cpx_N), orthopyroxene (Opx_N) and amphibole (Amp_N) in textural equilibrium with garnet (Grt_N). To fully describe the porphyroclastic and neoblastic assemblages and the different internal deformation microstructures, four different microstructural domains have been identified (Figures 3).

The Opx_P (domains 1 and 2; Figures 3a and b) varies in length from 1.5 to 3 mm and contains exsolution lamellae of garnet (Grt_E) clinopyroxene (Cpx_E) and amphibole (Amp_E). It shows intracrystalline deformation in the form of undulose extinction, kink bands, and core-and-mantle microstructures where the core of the porphyroclast grades outward into subgrains and newly recrystallized grains. The elongation of Opx_P is parallel to the trace of the compositional layering of the rock.

The coarse Cpx_P (domain 3; Figure 3c) displays undulose extinction and contains exsolution lamellae of Grt_E, orthopyroxene (Opx_E) and Amp_E. The Opx_E lamellae are 50-100 μm thick and up to 3 mm long, while Grt_E exsolutions are typically small with aspect ratios varying from 1:1 to 5:1. The exsolved Amp_E occurs as an interstitial phase at Cpx_P-Opx_E-Grt_E grain boundaries or triple junctions (Figure S2).

Both recrystallized Cpx_N and Opx_N (domain 4; Figure 3d) are optically strain-free and contain no exsolution lamellae. Garnet occurs as small crystals (up to 600 μm) in paragenesis with the neoblastic Cpx_N + Opx_N + Amp_N assemblage and defines the compositional layering of the rock. Notably, the garnet layering is parallel to the orientation of the garnet exsolution lamellae within orthopyroxene and clinopyroxene (Figure 3d).

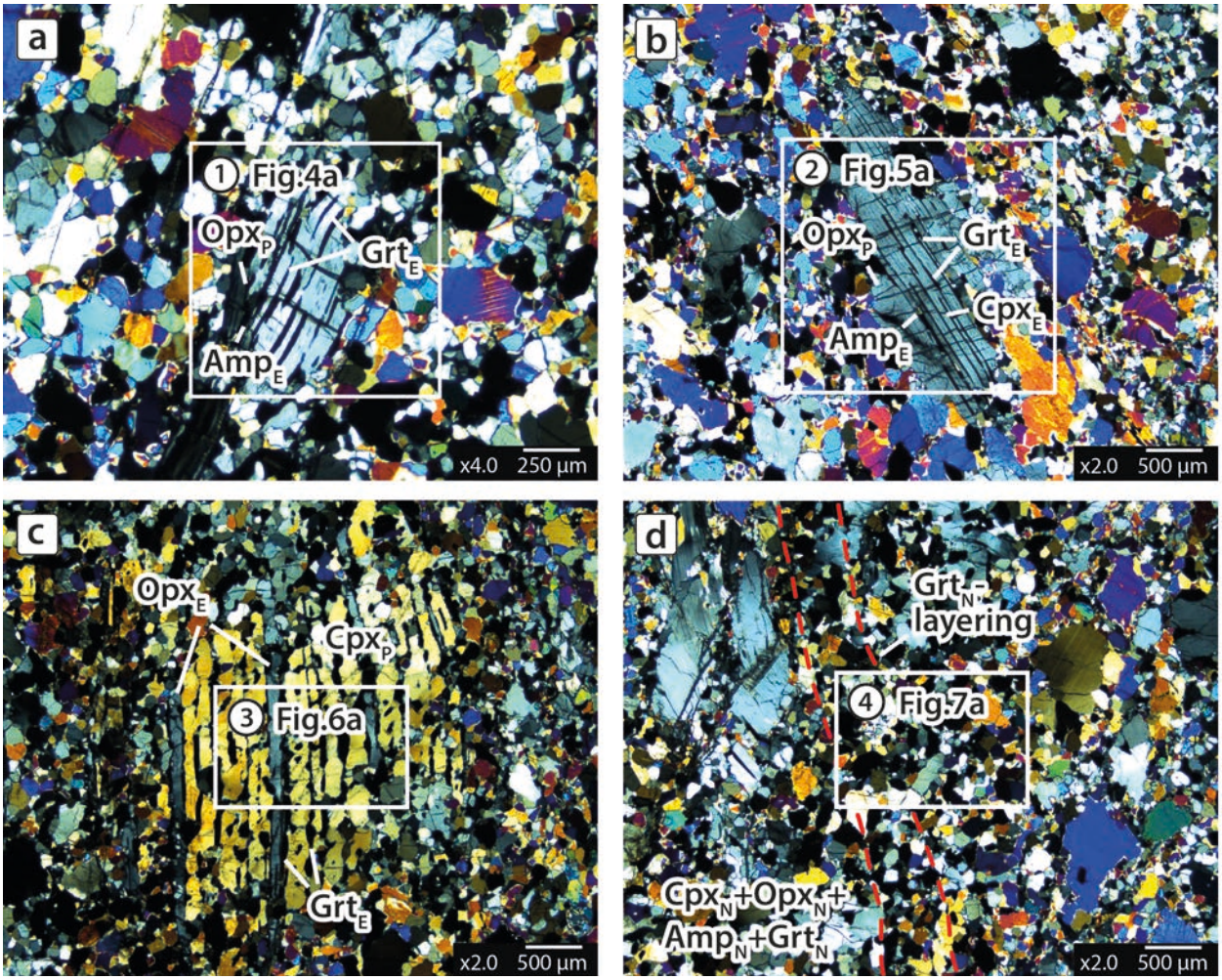

Figure 3. Photomicrographs of garnet websterites of Mt. Hochwart. XPL image of: (a) coarse Opx_P with Grt_E, and Amp_E exsolutions along curved crystal planes (sample UT23); (b) porphyroclastic Opx_P with exsolutions of Grt_E, Amp_E and Cpx_E (sample UT23); (c) porphyroclastic Cpx_P with exsolution lamellae of Grt_E and Opx_E (sample UT23); (d) Grt_N layering in garnet websterite UT23. The Grt_N layering is oriented parallel to the direction of the Grt_E exsolutions in Cpx_P. The white rectangles indicate the site of the EBSD maps shown in Figures 4 to 7. The circled numbers denote the microstructural domains. A large image of the texture of investigated westerites is provided in FigureS3.

4.3 EBSD analysis

The results of EBSD analysis of the different microstructural domains of garnet websterites are displayed in Figures 4 to 7 (see Figure 3 for the location of the EBSD maps):

(i) Domain 1 includes a deformed orthopyroxene porphyroclast surrounded by finer-grained recrystallized orthopyroxene neoblasts (Figure 3a);

(ii) Domain 2 shows a porphyroclastic orthopyroxene with a core-and-mantle microstructure (Figure 3b);

(iii) Domain 3 comprises a clinopyroxene porphyroclast (Figure 3c);

(iv) Domain 4 is representative of the recrystallized clinopyroxene grains around the porphyroclastic clinopyroxene of domain 3 (Figure 3d).

4.3.1 Domain 1

The coarse-grained Opx_P is oriented with the [010] axes subparallel to the stretching lineation and the (100) planes subparallel to the foliation (Figure 4b). The distortion of the crystal lattice is characterized by gradual increments of misorientations < 2° and with sharper misorientation jumps corresponding to low-angle boundaries (2°-10°), with a total distortion across the porphyroclast of 16° over a distance of 600 μm (profile AA' in Figure 4d). However, low-angle boundaries are scarce and are mostly restricted close to the garnet exsolutions (Figure 4a). The misorientation axes for low-angle misorientations shows two maxima close to the center of the pole figure and close to the pole to the foliation (Figure 4c). These misorientation axes preferentially cluster close to the [001] and the [100] axes in crystal coordinates (Figure 4c). The high-angle (> 10°) misorientation axes distributions resemble the patterns of the low-angle misorientation axes in sample and crystal coordinates (Figure 4c), but also show other minor clusters in different orientations, which are particularly evident in crystal coordinates. The misorientation angle distributions of correlated and uncorrelated pairs significantly deviate from the random theoretical curve. The correlated-pair distribution shows an excess in misorientation angles < 10° and a deficit in misorientation angles > 10°, while the uncorrelated-pair distribution shows higher frequency than the random-pair distribution for misorientations < 42° and lower frequency for misorientations > 42° (Figure 4e).

The transition from porphyroclastic Opx_P to the finer-grained, neoblastic Opx_N is marked by large misorientation angles between the new grains and the neighboring porphyroclast (profile BB' in Figure 4f). The recrystallized grains display common four-grain junctions (white arrow in Figure 4a), have internal misorientations lower than 3° (Figure S4) and are strongly misoriented with respect to each other (profile BB' in Figure 4f). The Opx_N has a weak CPO controlled by the parent porphyroclast (Figure 4b), showing a concentration of the [010] axes relatively close to the stretching lineation and a cluster of the (100) planes sub-parallel to the foliation (Figure 4b). The misorientation angle distribution of correlated pairs displays higher frequency than the random-pair distribution for misorientations < 60°, and lower frequency for misorientations > 60°. This pattern is evident also in the uncorrelated-pair distribution, but with smaller deviations from the random theoretical curve (Figure 4g).

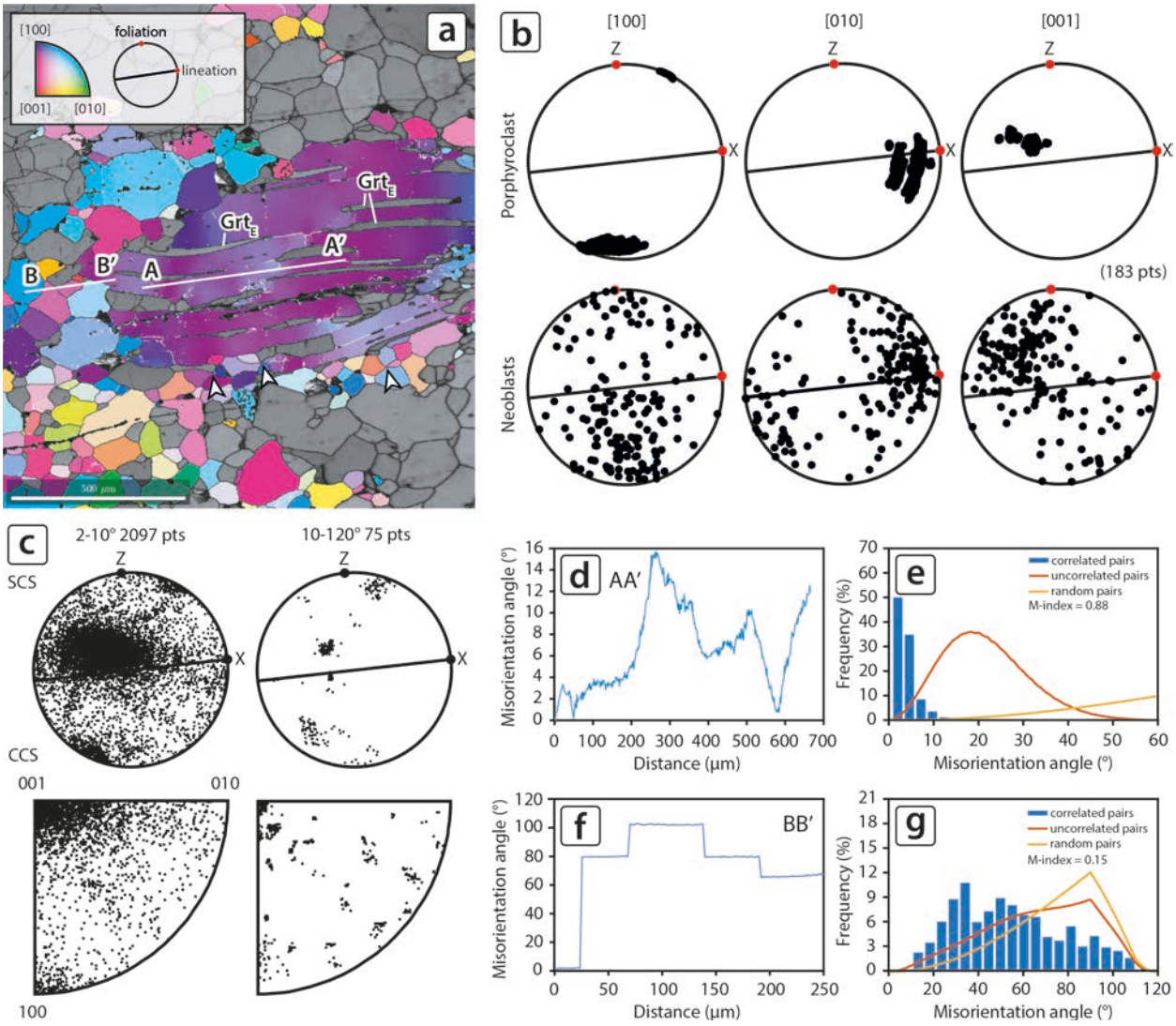

Figure 4. EBSD map and CPO data of Opx$_P$ and Opx$_N$ in garnet websterite UT23. (a) EBSD-derived inverse pole figure map with respect to Z sample direction. Grain boundaries are colored in black. Subgrain boundaries are colored in white. White arrows indicate the presence of four grain junctions in the recrystallized matrix; (b) pole figures of porphyroclastic (all data points) and neoblastic orthopyroxene. Upper hemisphere, equal area projection. Contoured plots are reported in Figure S5; (c) misorientation axis distributions for porphyroclastic orthopyroxene in sample (SCS, upper row) and crystal (CCS, lower row) coordinate system; (d) cumulative misorientations relative to the first point (profile AA'); (e) misorientation angle distribution for porphyroclastic orthopyroxene; (f) cumulative misorientations relative to the first point (profile BB'); (g) misorientation angle distribution for neoblastic orthopyroxene.

4.3.2 Domain 2

The porphyroclastic Opx$_P$ is oriented with the [010] axes subparallel to the stretching lineation and the (100) planes subparallel to the foliation (Figure 5b), consistently with the Opx$_P$ grain shown in Figure 4. The analyzed porphyroclast displays a strong internal distortion with

cumulative misorientations across the entire crystal as large as 32° (profile AA' in Figure 5d). However, low-angle boundaries are scarce and are mainly confined close to the margin of the porphyroclast. In sample coordinates, the misorientation axes distribution for low-angle misorientations displays a clear maximum close to the center of the pole figure, while in crystal coordinates, it forms a cluster close to [001] axis (Figure 5c). The high-angle misorientation axes in sample coordinates display a principal maximum close to (but slightly offset from) the center of the pole figure, and few minor scattered maxima, including a weak maximum close to the pole to the foliation (Figure 5c). In crystal coordinates, these misorientations axes preferentially cluster close to the [001] and [010] axes (Figure 5c). The misorientation angle distribution of correlated pairs shows higher frequency than the random-pair distribution for misorientations <10°, and lower frequency for misorientations >10°, while the uncorrelated pair distribution deviates from the random theoretical curve with an excess of misorientation angles < 40° and a deficit of misorientations for angles >40° (Figure 5e).

The transition from porphyroclastic to finer-grained, recrystallized Opx_N is marked by large misorientation angles, usually >20° (profile BB' in Figure 5f). The neoblastic Opx_N are almost strain-free (Figure S6), and have a CPO strongly controlled by the adjacent porphyroclast since they show the [010] axes aligned subparallel to the lineation and the (100) planes oriented subparallel to the foliation (Figure 5b). The misorientation angle distributions of both correlated and uncorrelated pairs show higher frequency than the random-pair distribution for misorientations <60°, and lower frequency for misorientations >60° (Figure 5g).

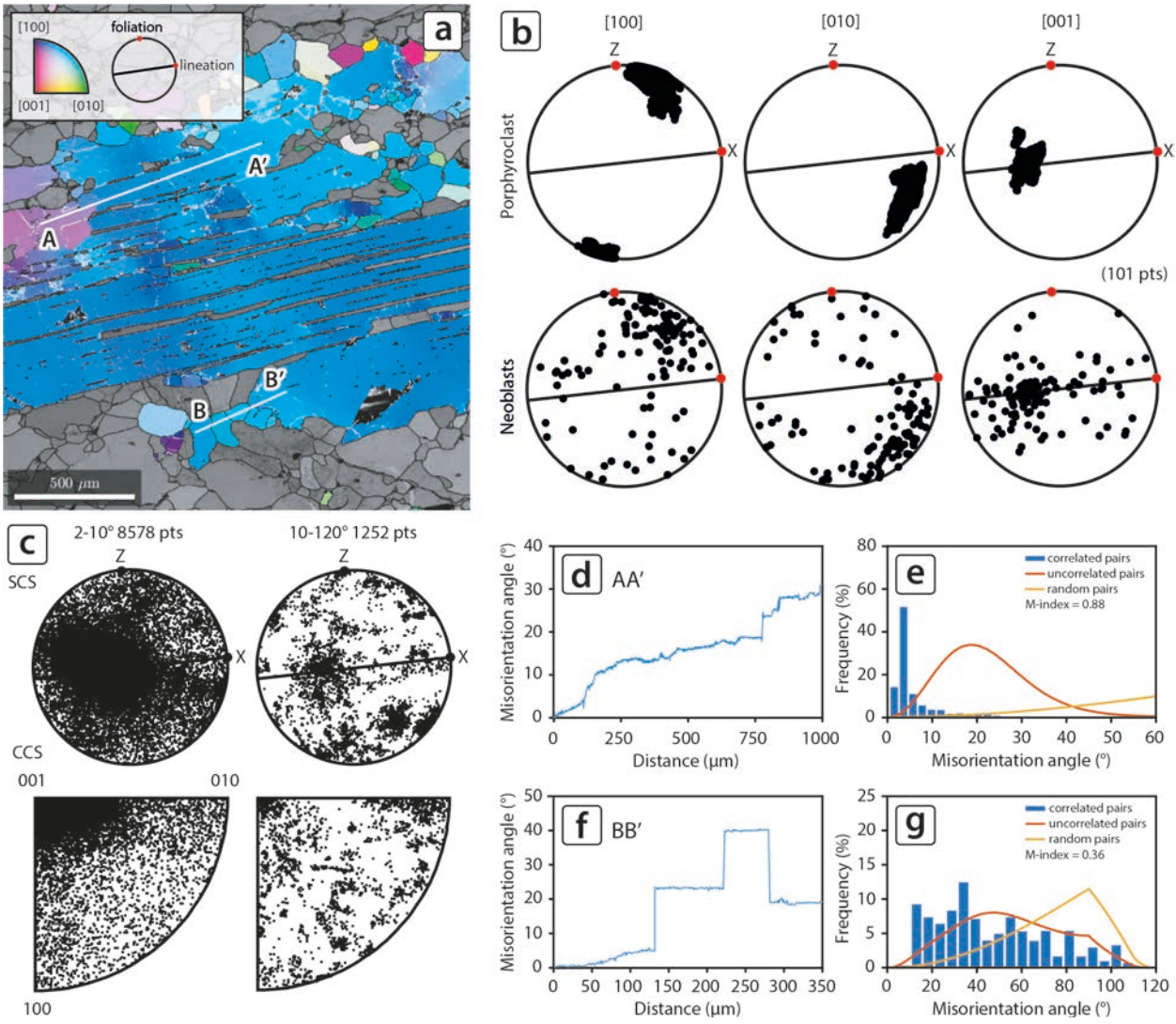

Figure 5. EBSD map and CPO data of Opx_P and Opx_N in garnet websterite UT23. (a) EBSD-derived inverse pole figure map with respect to Z sample direction. Grain boundaries are colored in black. Subgrain boundaries are colored in white; (b) pole figures of porphyroclastic (all data points) and neoblastic orthopyroxene. Upper hemisphere, equal area projection. Contoured plots are reported in Figure S7; (c) misorientation axis distributions in sample (upper row) and crystal (lower row) coordinate systems (abbreviations same as in Figure 4c); (d) cumulative misorientations relative to the first point (profile AA'); (e) misorientation angle distribution for porphyroclastic orthopyroxene; (f) cumulative misorientations relative to the first point (profile BB'); (g) misorientation angle distribution for neoblastic orthopyroxene.

4.3.3 Domain 3

Porphyroclastic Cpx_P is oriented with the [010] axes subparallel to the stretching lineation and the (100) planes subparallel to the foliation (Figure 6b). It displays an internal distortion with cumulative misorientations as large as 12° (profile AA' in Figure 6d). The density of low-angle boundaries is very low, consistently with a limited development of subgrains. The low-angle

misorientation axes in sample coordinates display a maximum close (but slightly offset from) to the center of the pole figures (Figure 6c). These misorientation axes cluster close to the [001] axis in crystal coordinates (Figure 6c). The high-angle misorientation axes distributions in both sample and crystal coordinates do not show any clear clustering (Figure 6c). The misorientation angle distributions of correlated and uncorrelated pairs show marked deviations from the random theoretical curve. The correlated-pair distribution shows an excess in misorientation angles <15° and a deficit in misorientation angles >15°, while the uncorrelated-pair distribution shows higher frequency than the random-pair distribution for misorientations <45° and lower frequency for misorientations >45° (Figure 6e).

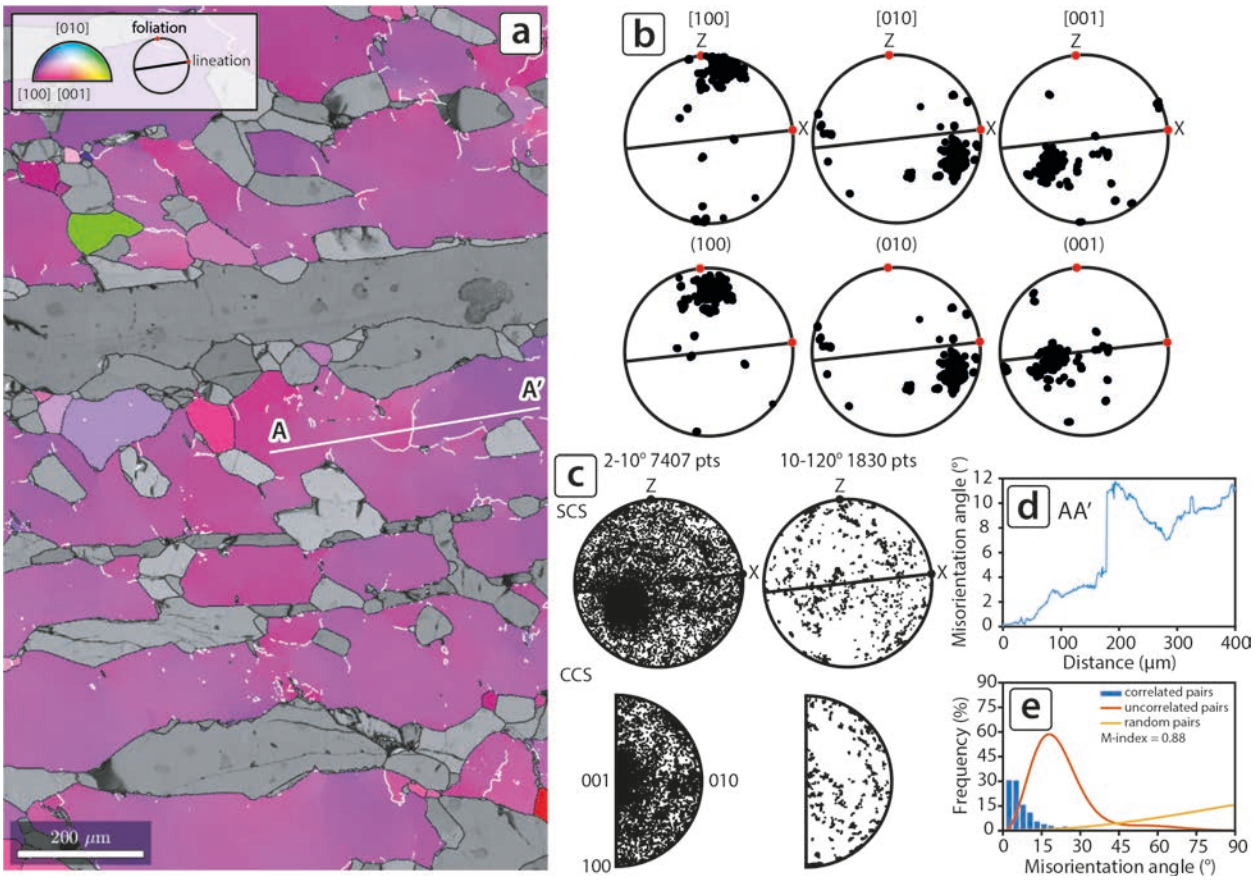

Figure 6. EBSD map and CPO data of Cpx_P in garnet websterite UT23. (a) EBSD-derived inverse pole figure map with respect to Z sample direction. Grain boundaries are colored in black. Subgrain boundaries are colored in white; (b) pole figures (all data points). Upper hemisphere, equal area projection; (c) misorientation axis distributions in sample (upper row) and crystal (lower row) coordinate systems (abbreviations same as in Figure 4c); (d) cumulative misorientations relative to the first point (profile AA'); (e) misorientation angle distributions.

4.3.4 Domain 4

The fine-grained Cpx_N displays a weak CPO slightly controlled by the CPO of the adjacent porphyroclast, showing a weak maximum of the [010] axes close to the stretching lineation and a concentration of the (100) planes subparallel to the foliation (Figure 7b). The fine-grained

aggregate of Cpx_N + Opx_N + Amp_N + Grt_N displays common four-grain junctions (Figures 7c and 7d) and aligned, straight grain boundaries (Figure 7e). The recrystallized clinopyroxene grains usually have internal misorientation lower than 3° (Figures 7c-f and S8) and are strongly misoriented with respect to each other (profile AA' in Figure 7f). The misorientation angle distributions of correlated and uncorrelated pairs deviate from the random theoretical curve showing an excess in misorientations angles lower than 90°, and a deficit in misorientation angles greater than 90° (Figure 7g).

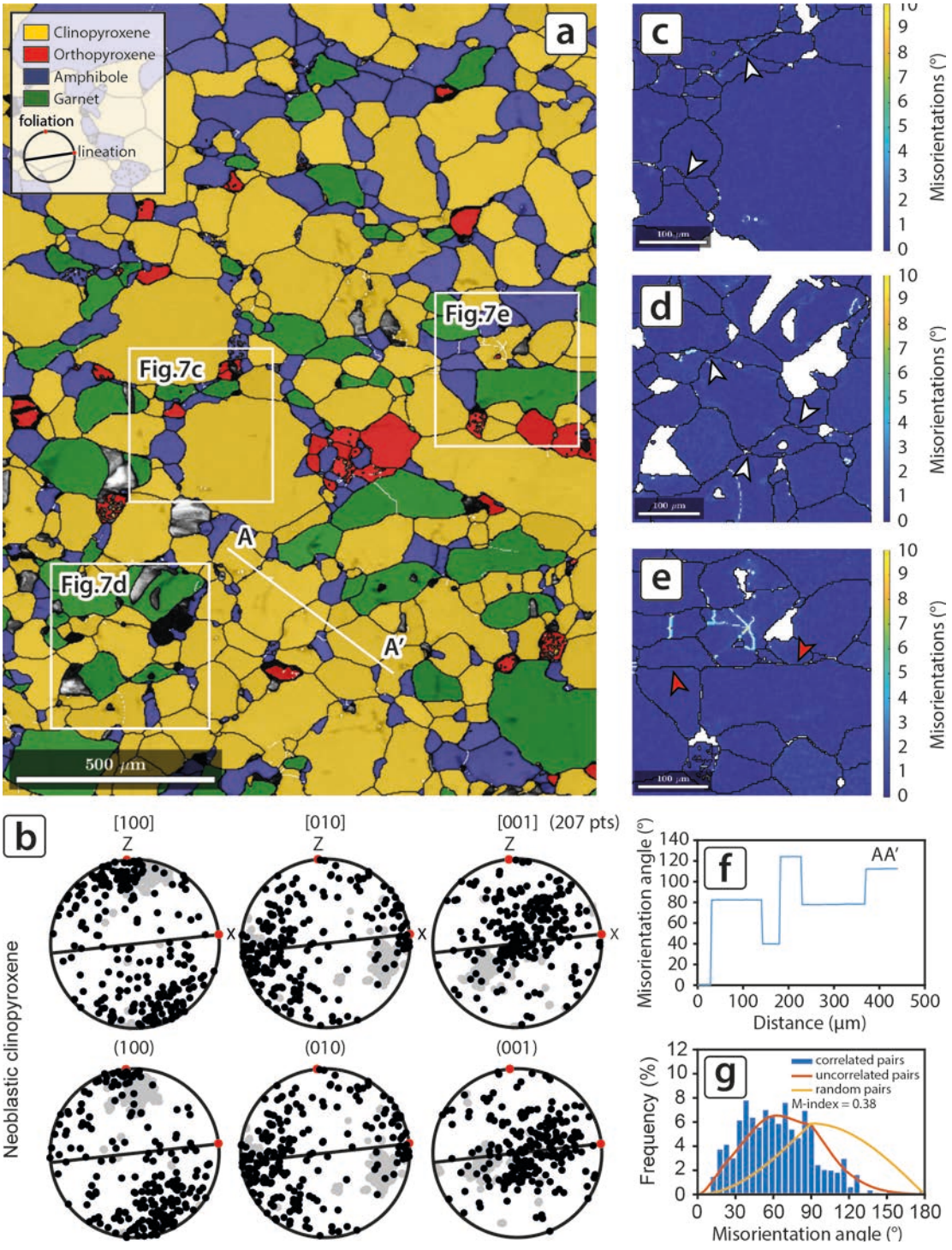

Figure 7. EBSD map and CPO data of the fine-grained matrix of garnet websterite UT23. The white rectangles indicate the sites of Figures 7c, 7d and 7e. (a) Phase map. Grain boundaries are colored in black. Subgrain boundaries are colored in white; (b) pole figures of neoblastic clinopyroxene in upper hemisphere, equal area projection. In light gray is reported the orientation of Cpx_P of domain 3. Contoured plots are reported in Figure S9; (c, d, e) local misorientation maps of the recrystallized matrix. Four grain junctions and aligned, straight grain boundaries are indicated by white and red arrows, respectively ; (f) cumulative misorientations of neoblastic clinopyroxene relative to the first point (profile AA'); (g) misorientation angle distributions of neoblastic clinopyroxene.

4.4 TEM characterization

Bright-field and dark-field TEM as well as STEM imaging were employed to observe lattice defects in orthopyroxene and to verify the slip systems that were activated during its deformation. Despite the distinct deformation of the host rock, orthopyroxene contains free dislocations only in moderate densities of $2\text{-}5 \cdot 10^{12}$ m^{-2} (Figure 8). STEM images show however that there are a number of sub-grain boundaries, which indicate that numerous dislocations climbed and recovered to form these internal boundaries (Figure 8b). The entire orthopyroxene is thus subdivided into a mosaic of several µm-sized sub-grains forming mutual low-angle boundaries between each other.

A closer look at the dislocation microstructures shows overall that dislocation lines are often similarly aligned, but at nodes dislocations meet also with different line directions, suggesting that not only one slip system was activated. To further evaluate the Burgers vector of the majority of dislocations, we have performed weak-beam TEM imaging using the $g \cdot b = 0$ criterion (Figure 8a). TEM images were systematically taken with reflections occurring in the [-112] zone axis diffraction pattern. When employing $g = 220$ (see Figure 8a), dislocations are well visible, excluding $b = [001]$ as Burgers vector. Dislocation are also well visible with $g = 0\text{-}21$, while they became invisible when using $g = 402$. In conclusion, this means that the Burgers vector of most dislocations is $b = [010]$, in line with EBSD measurements. The unequivocal determination of the slip plane turned out to be complicated because the mostly straight dislocation lines were strongly inclined to the beam direction, making an indexing of their directions difficult. Therefore, we used high-resolution imaging (HRTEM) to visualize in which plane the dislocation lines project. The lattice fringe image in Fig. 8c shows two projected dislocation lines that lie within the (100) plane, indicating this is the slip plane. Altogether the

444 TEM observations corroborate thus that the major slip system is (100)[010].

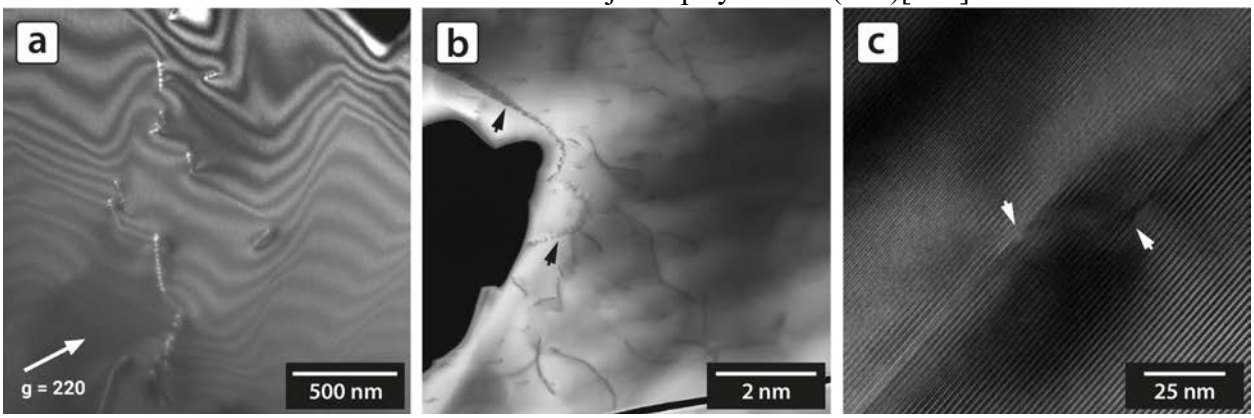

445

446

447 Figure 8. (a) Dark-field weak-beam, (b) LM-STEM dark-field and (c) high resolution TEM
448 images of dislocations in orthopyroxene from domain 2. Image (a) was taken with the 220
449 reflection, showing sharp well visible dislocations. The STEM image in (b) shows a larger and
450 thicker area of orthopyroxene with sub-grain boundaries (black arrows) and partly entangled
451 dislocations indicating interactions between them. The HRTEM image in (c) was taken along the
452 [0-13] zone axis and shows the 1.8 nm lattice fringes. Two dislocation lines are visible to lie in
453 projection in the (100) plane.

454

455 **5 Discussion**

456 **5.1 Deformation mechanisms**

457 The Opx_P is interpreted to deform by dislocation glide and creep on the (100)[010] slip system,
458 as indicated by microstructures, i.e. undulose extinction and crystal bending, the dominant [001]
459 misorientation axis, and by our TEM observations (Figure 8). Compared to the (100)[001],
460 which is considered the main activated slip system in orthopyroxene (Soustelle et al., 2009;
461 Tommasi et al., 2008; Skemer et al., 2006; Xu et al., 2006; Ishii & Sawaguchi, 2002; Vauchez
462 and Garrido, 2001; Mainprice et al., 2000; Christensen and Lundquist, 1982), the (100)[010] has
463 not been frequently reported in literature. However, rare natural occurrences (Jung et al., 2010;
464 Kohlstedt & Vander Sande, 1973; Nazè et al., 1987; Skrotzki, 1990, 1994), deformation
465 experiments (Nazè et al., 1987; Raleigh et al., 1971), room temperature indentations of enstatite
466 (Van Duysen et al., 1985), and numerical simulations (Jahn & Martonak, 2008), suggest that
467 orthopyroxene can deform and rotate around the [001] until the (100) tends to be parallel to the
468 XY foliation plane and the Burgers vector **b** [010] becomes parallel to the stretching lineation, as
469 observed in our orthopyroxene porphyroclasts.

470 The core-and-mantle microstructure of Opx_P of domain 2 suggests that dislocation creep on the
471 (100)[010] was accommodated by subgrain rotation (SGR) recrystallization. In particular, we
472 observe that low-angle boundaries are mostly restricted close to the rim of the porphyroclast,
473 reflecting a progressive accumulation of misorientations from the core of the Opx_P to the mantle
474 of the newly recrystallized grains.

475 The recrystallized Opx_N is interpreted to deform primarily by grain boundary sliding (GBS), as
476 indicated by the common occurrence of four-grain junctions in the recrystallized Opx_N matrix

(Figure 4a). The Opx_N locally forms a mosaic-like texture with 120° triple junctions suggesting that annealing and grain growth occur during/after deformation by GBS. This is also supported by the average grain size of the recrystallized Opx_N (76.5 μm), which is slightly larger than the average size of the internal subgrains of porphyroclastic Opx_P (58.5 μm; Table S1).

The Cpx_P porphyroclast shows an orientation (Figure 6b) which is consistent with dislocation glide and creep on the (100)[010] slip system, as also indicated by the low-angle misorientation axes distributions in crystal coordinates (Figure 6c). Most of the studies on clinopyroxene CPOs concern omphacite, and indicate that the dominant slip systems are (100)[001], {110}[001] and {110}½<110> (e.g. Godard and van Roermund, 1995; Bascou et al., 2002; Ulrich and Mainprice, 2005; Raterron et al., 2014; Zhang et al., 2006), which combined together can result in the S-type, L-type and SL-type CPOs. Whilst the (100)[001], {110}[001] and {1-10}½<110> slip systems have been frequently reported in both naturally and experimentally deformed clinopyroxenes at variable pressure, temperature, and water content conditions (e.g. Bascou et al., 2001, 2002; Bystricky & Mackwell, 2001; Frets et al., 2012; Godard & van Roermund, 1995; Raterron et al., 2014; Ulrich & Mainprice, 2005), the (100)[010] slip system has been only rarely observed in deformation experiments (Van Duysen & Doukhan, 1984), room temperature indentations of spodumene (Doukhan et al., 1986; Van Duysen & Doukhan, 1984), and naturally deformed augites (Skrotzki, 1994).

The recrystallized Cpx_N shows evidence for GBS, including the occurrence of four-grain junctions (Figures 7c and 7d) and aligned, straight grain boundaries in the recrystallized Cpx_N matrix (Figure 7e). In particular, the four-grain junctions represent evidence for grain neighbor switching during GBS (Ashby & Verrall, 1973; Maruyama & Hiraga, 2017), while straight grain boundaries represent the sliding surfaces that were active during the relative movement of neighbor grains (Boullier & Gueguen, 1975; Miranda et al., 2016; White, 1977, 1979). In addition, the movement of grains during neighbor switching requires a rotational component of motion, which produces an increase in misorientations between adjacent grains (e.g. Bestmann & Prior, 2003; Svahnberg & Piazolo, 2010). This is consistent with our observation of large misorientation angles between neighbor recrystallized Cpx_N (Figure 7f). In summary, our microstructural observations, together with the low internal strain and the dispersion of CPO and misorientation axes for large misorientations, suggest that the main deformation mechanism of Opx_N and Cpx_N was diffusion accommodated GBS (i.e. diffusion creep).

5.2 Piezometry and rheological model

In this section we report the effects of the transformation of the coarse-grained Opx_P and Cpx_P into the finer-grained Opx_N and Cpx_N on the bulk rheology of the UZ garnet websterites. Based on the deformation mechanisms identified from microstructures, i.e. dislocation glide and creep in the porphyroclasts, and diffusion creep in the finer-grained neoblasts, deformation mechanism maps have been calculated for ortho- and clinopyroxene, and plotted as grain size versus differential stress and differential stress versus strain rate diagrams (Figure 10).

The flow law of Bystricky et al., (2016) has been used to calculate the dislocation creep component of the total strain rate for orthopyroxene:

$$\dot{\varepsilon} = A_{dis}\, \sigma^{n_{dis}}\, e^{-\frac{Q_{dis}}{RT}} \qquad (1)$$

519

520 where $\dot{\varepsilon}$ is the strain rate (s^{-1}), σ is the differential stress (MPa), n is the stress exponent, T is the
521 temperature (K), R is the gas constant ($JK^{-1}mol^{-1}$), and A_{dis}, ($MPa^{-3}s^{-1}$) n_{dis} and Q_{dis} ($Jmol^{-1}$) are
522 empirical parameters for the pre-exponential term, the stress exponent, and the activation energy
523 for dislocation creep, respectively.

524 The contribution of diffusion creep in orthopyroxene has been calculated using the flow law
525 proposed by Bruijn and Skemer, (2014):

526

527 $$\dot{\varepsilon} = C_m(T)\ \sigma\ d^{-p} \qquad (2)$$

528

529 where $\dot{\varepsilon}$ is the strain rate (s^{-1}), σ is the differential stress (MPa), C_m(T) is the temperature-
530 dependent variable ($s^{-1}MPa^{-1}\mu m^3$), d is the grain size (μm), and p is the grain size exponent.

531 Differential stress during deformation was estimated using the grain size piezometer for
532 orthopyroxene of Linckens et al., (2014):

533

534 $$\sigma_{diff} = 2939\ d^{-1.308} \qquad (3)$$

535

536 where σ_{diff} is the differential stress in MPa, and d is the grain size in μm.

537 The flow law of Dimanov and Dresen, (2005) has been used to calculate the contribution of
538 dislocation creep and diffusion creep to the total strain rate for clinopyroxene:

539

540 $$\dot{\varepsilon} = A_{gss}\ \sigma^{n_{gss}}\ d^{-m}\ e^{-\frac{Q_{gss}}{RT}} + A_{gsi}\ \sigma^{n_{gsi}}\ e^{-\frac{Q_{gsi}}{RT}} \qquad (4)$$

541

542 where $\dot{\varepsilon}$ is the strain rate (s^{-1}), A is the pre-exponential constant (given in $Pa^{-n}s^{-1}$ for GSI creep
543 and $Pa^{-n}s^{-1}m^3$ for GSS creep; see caption of Table S2), σ is the differential stress (Pa), n is the
544 stress exponent, d is the grain size (m), m is the grain size exponent, Q is the activation energy
545 ($Jmol^{-1}$), R is the molar gas constant ($JK^{-1}mol^{-1}$) and T is the absolute temperature (K). The
546 subscripts *gss* and *gsi* indicate the grain size sensitive (i.e. diffusion creep) and the grain size
547 insensitive (i.e. dislocation creep) components of the total strain rate $\dot{\varepsilon}$. All the parameters used
548 for calculation of deformation mechanism maps are given in Table S2 of supporting information.

549 Microstructures and crystallographic orientation data suggest that the transition from dislocation
550 to diffusion creep in garnet websterites was promoted by the transformation of the coarse-
551 grained Opx_P and Cpx_P into the finer-grained Opx_N and Cpx_N. The switch in the deformation
552 mechanism and the reduction of the grain size were also accompanied by the crystallization of
553 garnet as exsolutions in high-T pyroxene porphyroclasts, and as neoblasts in textural equilibrium
554 with the finer-grained Cpx_N + Opx_N + Amp_N matrix, indicating that deformation probably took
555 place at high-pressure (HP) conditions.

To better constrain the P-T conditions at which deformation occurred, we calculated a P-T isochemical section (Figure 9) using the composition of garnet websterite UT23 (caption of Figure 9). Results indicate that the Cpx_N + Opx_N + Amp_N + Grt_N assemblage observed in the recrystallized matrix of garnet websterites is thermodynamically stable at pressure from 1.5 to 3.0 GPa and temperature ranging from 750 °C to 1100 °C (Figure 9). In particular, following the prograde P-T path of the ultramafic rocks of the UZ reported in Figure 9 (Nimis & Morten, 2000), the Cpx_N + Opx_N + Amp_N + Grt_N assemblage is expected to form at ca. 2 GPa and 850 °C. Therefore, the shift from porphyroclastic to neoblastic assemblage and the switch in the deformation mechanism are interpreted to have occurred when garnet websterites, after a stage of isobaric cooling, crossed the garnet-in reaction curve at ca. 2 GPa and 850 °C (Figure 9) prior to be dragged to greater depths at nearly constant temperature. Also, at these conditions garnet websterites are expected to be composed by 47 vol% of orthopyroxene and 30 vol% of clinopyroxene (Figure 9).

Thus, to describe the deformational behavior of the investigated garnet websterites, flow laws and deformation mechanism maps have been calculated at 2 GPa and T=850°C. Many petrological studies also suggest that at these conditions, metamorphism in the UZ was accompanied by intense fluid infiltration (e.g. Tumiati et al. 2003, 2007). This is consistent with our observation of amphibole (Amp_N) in textural equilibrium with the Cpx_N + Opx_N + Grt_N assemblage, indicating that recrystallization and deformation occurred in presence of H_2O. Despite this, the occurrence of amphibole in the recrystallized matrix does not imply the presence of intracrystalline H_2O in Cpx_N and Opx_N. Hence, to fully describe the deformational behavior of our garnet websterites, we calculated flow laws and deformation mechanism maps both for dry and wet conditions. As no flow laws are available for wet orthopyroxene, we investigated the rheology of the garnet websterites using the flow laws for dry orthopyroxene (Bruijn & Skemer, 2014; Bystricky et al., 2016) and for dry and wet clinopyroxene (Dimanov & Dresen, 2005).

In Figure 10a, a differential stress of 14 MPa was estimated from the subgrain size of Opx_P (58.5 μm). Assuming that the differential stress is representative of the bulk flow stress, deformation by dislocation creep in Opx_P would occur at strain rates of 2.4×10^{-16} s^{-1} (Figure 10a). Assuming that deformation evolved at constant stress, this transition results in a rheological weakening, as Opx_N would deform at faster strain rates than those estimated for the formation of subgrains in Opx_P. However, we note that the average grain size of Opx_N is slightly larger than the subgrain size. We attribute this to partial annealing and grain growth of Opx_N, yet this grain size plots close to the transition between the different deformation regimes. It is likely that grain growth and annealing were limited by the syn-kinematic nucleation of second phases, which kept the grain size sufficiently small for the local activity of diffusion creep.

Figure 10b shows the curves describing the rheological behavior of Opx_N and Cpx_N. For the range of differential stress estimated from the subgrain size in Opx_N, the Cpx_N would deform via diffusion creep at strain rates of 3.9×10^{-15} s^{-1} and 2.7×10^{-12} s^{-1} at dry and wet conditions, respectively. Furthermore, the relative proportions of Opx_N (47 vol%) and Cpx_N (30 vol%) estimated by thermodynamic model of Figure 9, indicate the bulk deformation would be controlled by the strength of the weaker phase (e.g. Handy, 1990), i.e. the Cpx_N, which is expected to flow at faster strain rates than Opx_N both under dry and wet conditions.

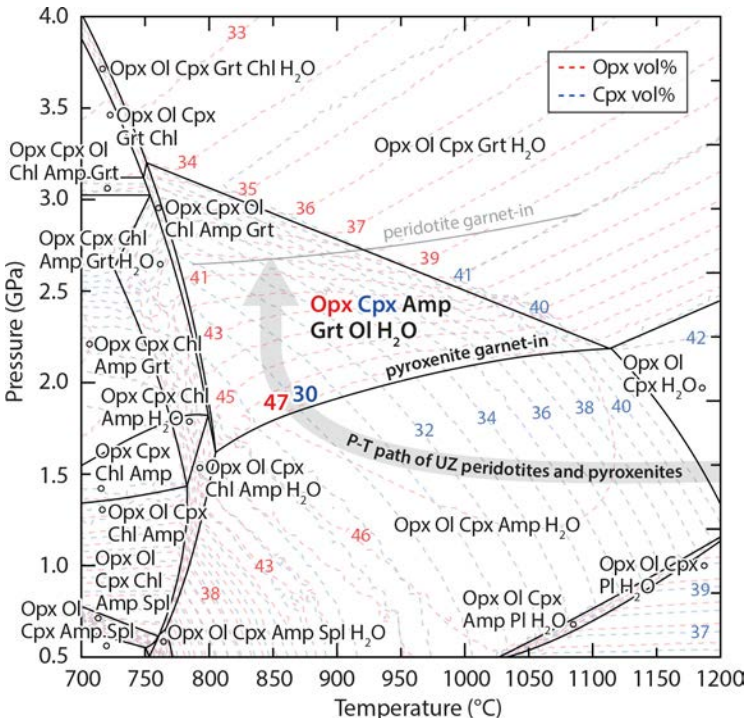

Figure 9. P-T isochemical section at H_2O saturated condition of the garnet websterite UT23 (composition in wt.%: Na_2O=0.60, MgO=23.91, Al_2O_3=5.93, SiO_2=50.62, K_2O=0.06, CaO=9.94, FeO=5.35; a detailed description of the working conditions during inductively-coupled plasma mass spectrometry (ICP-MS) and LECO combustion (total C, S) analyses is given in Text S2). The compositions of Opx, Cpx, Grt and Amp calculated from thermodynamic modelling are reported in Table S3. Thin dashed red and blue lines represent the isopleths of orthopyroxene and clinopyroxene volume fractions (vol%), respectively. The thin gray line is the garnet-in curve of UZ peridotites from Nimis and Morten, (2000). The thick transparent gray line is the P-T path of UZ pyroxenites and peridotites (Nimis and Morten, 2000).

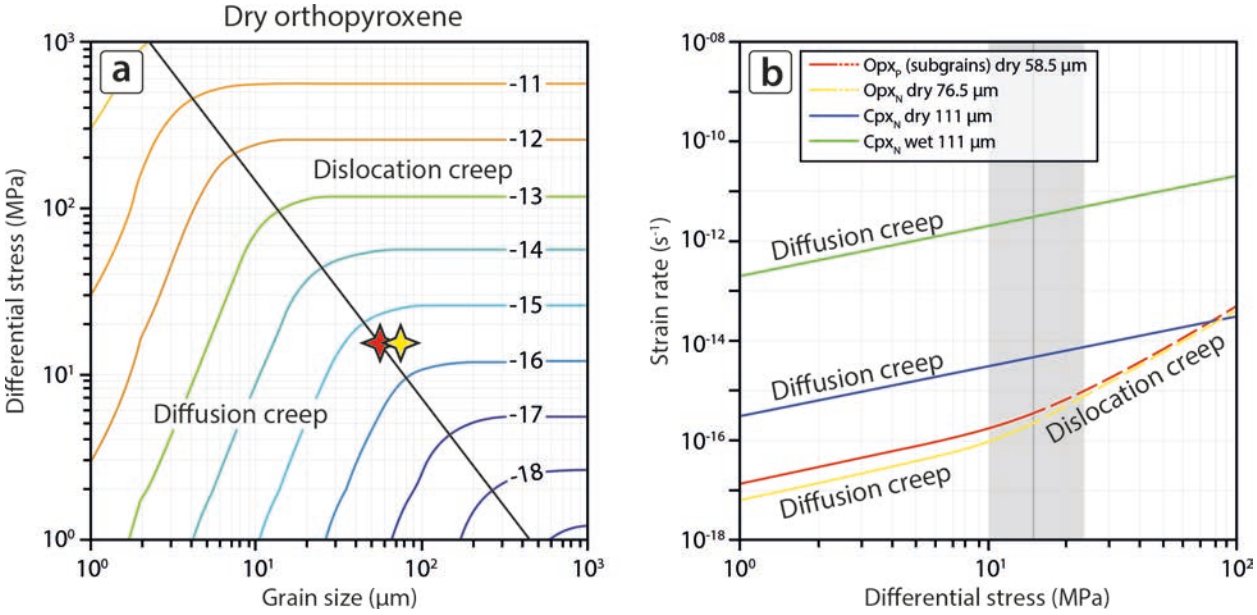

Figure 10. (a) Grain size vs differential stress map with contoured strain rate curves for dry orthopyroxene. The black solid line is the piezometer by Linckens et al., (2014). The red stars correspond to the size of subgrains in Opx_P (58.5 μm) while the yellow star represent the recrystallized Opx_N (76.5 μm); (b) strain rate vs. differential stress diagram reporting the curves calculated for orthopyroxene (only dry) and clinopyroxene (wet and dry). The red line is the curve calculated for subgrains in Opx_P (58.5 μm). The yellow curve represent the recrystallized Opx_N (76.5 μm). Solid and dashed curves describe the deformational behavior of orthopyroxene in the diffusion creep and dislocation creep regimes, respectively. The green solid and dashed curves have been calculated for recrystallized Cpx_N (111 μm) at dry and wet conditions, respectively. The gray transparent field (width include errors) represent the differential stress calculated by the orthopyroxene piezometer by Linckens et al., (2014). Deformation mechanism maps have been calculated at 850 °C. Other details on the derivation of the deformation mechanism maps are given in section 4.2 of the main text and in Table S2.

5.3 The role of pyroxenites in mantle weakening

Pyroxenites are important constituents of the upper mantle and, despite their low volumetric abundance, represent key lithologies in mantle deformation processes since compositional heterogeneities can play a major role in strain localization and weakening (e.g. Tommasi et al., 2015; Tikoff et al., 2010; Toy et al., 2010; Treagus & Sokoutis, 1992).

The origin of pyroxenites has been related to a variety of magmatic and metamorphic processes, including: i) recycling of crustal material during subduction (Allègre & Turcotte, 1986; Kornprobst et al., 1990; Morishita & Arai, 2001; Morishita et al., 2003; Yu et al., 2010); ii) moderate- to high-pressure crystal segregation from magmas rising from asthenospheric mantle sources (Bodinier et al., 1987a, 1987b; Dantas et al., 2007; Gysi et al., 2011; Kempton & Stephens, 1997; Keshav et al., 2007; Mukasa & Shervais, 1999; Rivalenti et al., 1995; Takazawa et al., 1999; Vannucci et al., 1993; Warren et al., 2009); iii) refertilization of 'depleted' upper mantle through melt-peridotite reactions during asthenospheric upwelling (Bodinier et al., 2008; Dantas et al., 2009; Garrido & Bodinier, 1999; Van Acken et al., 2010); and iv) reaction between peridotites and melts derived by high-pressure melting of the subducted crust (e.g. Malaspina et al., 2006; Pellegrino et al., 2020; Wang et al., 2008;).

Pyroxenites occur ubiquitously in most of oceanic and orogenic peridotite massifs, such as Lherz in the Pyrenees, Beni Bousera and Ronda in the Betic-Rif belt, Lanzo, Erro-Tobbio, Monte Duria, and Ulten Zone in the Alps (Bodinier et al., 2008; Dickey, 1970; Garrido and Bodinier, 1999; Gysi et al., 2011; Kornprobst, 1969, 1970; Morten & Obata, 1983; Rampone & Borghini, 2008; Tumiati et al., 2018). The studied pyroxenites occurring in the UZ have been interpreted as crystal segregation from a basaltic melt rising from the deeper portions of the mantle wedge (Nimis and Morten, 2000). These pyroxenites record a mineral phase transformation from coarse-grained websterites to finer-grained garnet websterites (Morten and Obata, 1983; Nimis and Morten, 2000). Host peridotites record a similar evolution from coarse protogranular spinel lherzolites to fine-grained amphibole + garnet peridotites (Obata and Morten, 1987). This coupled evolution has been interpreted to reflect pressure increase and cooling of websterites and host peridotites from spinel- (1200 °C, 1.3-1.6 GPa) to garnet-facies (850 °C and 2.7 GPa) conditions induced by mantle corner flow (Nimis and Morten, 2000).

Microstructures indicate that the re-equilibration of garnet websterites in the garnet stability field was accompanied by a strong reduction of the grain size with the consequent switch of the deformation mechanism from dislocation creep in the porphyroclasts to diffusion creep in the finer-grained neoblasts, resulting in rheological weakening. However, grain size reduction could be not sufficient to cause a permanent transition from dislocation to diffusion creep because of grain growth (De Bresser et al., 2001), unless the latter is inhibited by other processes such as metamorphic reactions (e.g. Newman et al., 1999). In the investigated samples, the reduction of the grain size was assisted by the crystallization of garnet in response to the re-equilibration of garnet websterites in the garnet stability field. In particular, garnet exsolved from coarse-grained pyroxenes contributing to the reduction of the grain size through the progressive disruption of the porphyroclastic assemblage, and crystallized along the garnet websterite foliation facilitating the pinning of the recrystallized matrix and stabilizing the fine-grained microtexture for diffusion creep and rheological weakening.

It is demonstrated that syn-deformational metamorphic reactions, such as the breakdown of a mantle aluminous phase (i.e. plagioclase, spinel and garnet), can promote a switch to diffusion creep and the associated weakening in the upper mantle (e.g. Furusho & Kanagawa, 1999; Newman et al., 1999). The stability of these aluminous phases is strongly affected by major-elements composition and, at fixed P-T conditions, pyroxenites and peridotites can develop different phase assemblages as a result of different compositions (e.g. Schmädicke, 2000). Numerous experimental studies have also demonstrated that garnet forms at lower pressures in pyroxenites with respect to peridotites (e.g., Adam et al., 1992; Borghini & Fumagalli, 2018; Irving, 1974). Therefore, during the prograde path of UZ mantle rocks towards the slab-mantle interface, the reduction of the grain size, the switch in the deformation mechanism, and the rheological weakening associated with the transition to garnet-facies conditions, would occur at shallower depths in websterites compared to the host peridotite. This indicates that compositional variations (e.g. websterites) may also represent rheological heterogeneities where weakening and deformation can localize, thus suggesting that the distribution and the degree of deformation in the upper mantle may be strongly controlled by the presence and the volumetric fraction of compositional heterogeneities such as websterites.

Similar processes have been also documented by Hidas et al. (2013) in the Ronda Peridotite massif. There, rheological weakening of thin pyroxenite layers was associated with a decrease of the grain size and an increase of the volume fraction of plagioclase in response to the spinel to plagioclase phase transformation reaction, which induces the activation of GSS creep mechanisms and the rheological weakening of the pyroxenite bands that also affects the host peridotite. Our study demonstrates that reaction weakening can occur not only during the exhumation of the subcontinental mantle, but also during its burial towards the slab interface in response to the corner flow.

The schematic illustration of Figure 11 reports a conceptual model for the weakening of garnet websterites during the mantle corner flow. At high-temperature and low-pressure (1 in Figure 11), spinel lherzolites are intruded by melts rising from the deeper portions of the wedge, leading to the formation of coarse-grained websterites (e.g. Morten & Obata, 1983) characterized by large (up to 6 cm), high-T, tschermakitic pyroxenes (c.f. Table S3 and Nimis & Morten, 2000). Mantle convection (solid grey lines in Figure 11) induced by the movement of the subducting plate causes cooling and pressure increase of websterites while moving towards the slab-mantle interface (path from 1 to 2 in Figure 11). Cooling and pressure increase induces the solid-state

exsolution of garnet by removing the Tschermak component from the coarse, high-T, tschermakitic pyroxenes (Gasparik, 1990; Spengler et al., 2012), and the crystallization of garnet along the websterite foliation. At this stage, syn-kinematic exsolution reactions are accompanied by dislocation creep and dynamic recrystallization of pyroxene porphyroclasts. This produces a reduction of the grain size triggering a transition in deformation mechanism from dislocation creep to diffusion creep. The associated weakening of garnet websterites likely created favorable conditions for the incorporation of garnet websterites and host peridotites into the subducting crust.

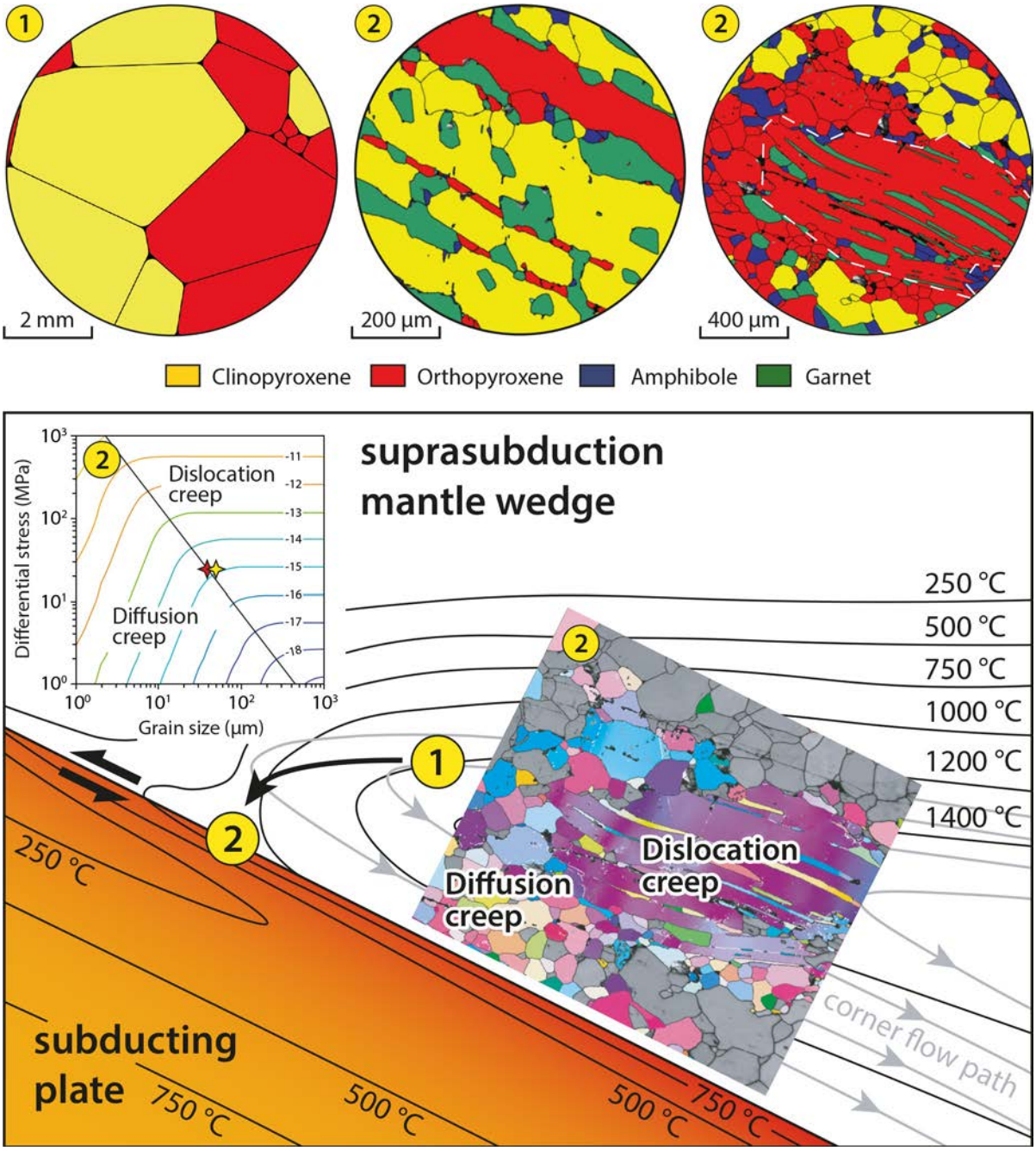

Figure 11. Conceptual model for mantle weakening induced by mantle corner flow (not to scale). See text for explanation. Model thermal configuration after Honda (1985). Black bold line: metamorphic path of garnet websterites of UZ. Solid grey lines: mantle corner flow path.

6 Conclusions

The re-equilibration of websterites of UZ in the garnet stability field occurred under a deformation regime. Microstructures, EBSD data, and TEM investigations suggest that pyroxene porphyroclasts dominantly deformed by recrystallization-accommodated dislocation creep on the (100)[010] slip system, while the recrystallized pyroxene grains record deformation by dominant diffusion-accommodated grain boundary sliding.

Thermodynamic modelling indicates that the transition from dislocation creep to diffusion creep likely took place at 2 GPa and 850 °C during the prograde re-equilibration of websterites in the garnet stability field. During the cooling from 1200 to 850 °C, the Al-rich porphyroclastic pyroxenes exsolved garnet along the cleavages, which progressively crystallized forming the garnet websterite foliation, then triggering the pinning of the recrystallized matrix and stabilizing the fine-grained microtexture for diffusion creep. The activation of the diffusion creep induced a significant rheological weakening in the garnet websterites, that also affected the host peridotite, thus suggesting that the occurrence of compositional heterogeneities, e.g. pyroxenites l.s., can have important effect on the bulk rheological behavior of the upper mantle.

Acknowledgments, Samples, and Data

The authors declare no competing financial interests.

The supporting information and the data set for this study can be find at the doi:10.17632/shvnp5hdp4.1

The staff of the University of Plymouth Electron Microscopy Centre is thanked for assistance during EBSD data acquisition. We also thank A. Risplendente for the support during electron microprobe analyses. This work was funded by the Italian Ministry of University and Research (PRIN 2017 - Prot. 2017ZE49E7_005 - The Dynamic Mass Transfer from Slabs to Arcs - Dynastars and MIUR-DAAD Joint Mobility Program - The redox state of the Earth's mantle: from the slab-mantle interface to the sub-continental lithosphere). This work also benefited from Erasmus Plus Traineeship program. F.L. is grateful to the Deutsche Forschungsgemeinschaft for funding the TEM facilities via the Gottfried-Wilhelm-Leibniz programme (LA830/14-1). M. Campione is thanked for stimulating discussions and A. Ceccato for help with rheological calculations and EBSD data post processing with Channel5.

References

Adam, J., Green, T. H., & Day, R. A. (1992). An experimental study of two garnet pyroxenite xenoliths from the Bullenmerri and Gnotuk Maars of western Victoria, Australia. *Contributions to Mineralogy and Petrology, 111*(4), 505-514. doi:10.1007/BF00320905

Allègre, C. J., & Turcotte, D. L. (1986). Implications of a two-component marble-cake mantle. *Nature, 323*(6084), 123-127. doi:10.1038/323123a0

745 Ashby, M. F., & Verrall, R. A. (1973). Diffusion-accommodated flow and superplasticity. *Acta*
746 *metallurgica, 21*(2), 149-163. doi:10.1016/0001-6160(73)90057-6

747 Avé Lallemant, H. G. (1978). Experimental deformation of diopside and websterite.
748 *Tectonophysics, 48*(1-2), 1-27. doi:10.1016/0040-1951(78)90083-5

749 Bachmann, F., Hielscher, R., & Schaeben, H. (2010). Texture Analysis with MTEX-Free and
750 Open Source Software Toolbox. *Solid State Phenomena, 160*, 63–68.
751 doi:10.4028/www.scientific.net/SSP.160.63

752 Bai, Q., & Kohlstedt, D. L. (1992). High-temperature creep of olivine single crystals III.
753 Mechanical results for unbuffered samples and creep mechanisms. *Philosophical Magazine A,*
754 *66*(6), 1149-1181. doi:10.1080/01418619208248011

755 Bascou, J., Barruol, G., Vauchez, A., Mainprice, D., & Egydio-Silva, M. (2001). EBSD-
756 measured lattice-preferred orientations and seismic properties of eclogites. *Tectonophysics,*
757 *342(1-2)*, 61-80. doi:10.1016/S0040-1951(01)00156-1

758 Bascou, J., Tommasi, A., & Mainprice, D. (2002). Plastic deformation and development of
759 clinopyroxene lattice preferred orientations in eclogites. *Journal of Structural Geology, 24*(8),
760 1357-1368. doi:10.1016/S0191-8141(01)00137-7

761 Bestmann, M., & Prior, D. J. (2003). Intragranular dynamic recrystallization in naturally
762 deformed calcite marble: diffusion accommodated grain boundary sliding as a result of subgrain
763 rotation recrystallization. *Journal of Structural Geology, 25*(10), 1597-1613. doi:10.1016/S0191-
764 8141(03)00006-3

765 Bodinier, J. L., Fabriès, J., Lorand, J. P., Dostal, J., & Dupuy, C. (1987a). Geochemistry of
766 amphibole pyroxenite veins from the Lherz and Freychinede ultramafic bodies (Ariege, French
767 Pyrenees). *Bulletin de minéralogie, 110*(4), 345-358.

768 Bodinier, J. L., Guiraud, M., Fabries, J., Dostal, J., & Dupuy, C. (1987). Petrogenesis of layered
769 pyroxenites from the Lherz, Freychinede and Prades ultramafic bodies (Ariege, French
770 Pyrenees). *Geochimica et Cosmochimica Acta, 51*(2), 279-290. doi:10.1016/0016-
771 7037(87)90240-7

772 Bodinier, J. L., Garrido, C. J., Chanefo, I., Bruguier, O., & Gervilla, F. (2008). Origin of
773 pyroxenite–peridotite veined mantle by refertilization reactions: evidence from the Ronda
774 peridotite (Southern Spain). *Journal of Petrology, 49*(5), 999-1025.
775 doi:10.1093/petrology/egn014

776 Borghini, G., Fumagalli, P., & Rampone, E. (2010). The stability of plagioclase in the upper
777 mantle: subsolidus experiments on fertile and depleted lherzolite. *Journal of Petrology, 51*(1-2),
778 229-254. doi:10.1093/petrology/egp079

779 Borghini, G., & Fumagalli, P. (2018). Subsolidus phase relations in a mantle pyroxenite: an
780 experimental study from 0.7 to 1.5 GPa. *European Journal of Mineralogy, 30*(2), 333-348.
781 doi:10.1127/ejm/2018/0030-2735

782 Boullier, A. M., & Gueguen, Y. (1975). SP-mylonites: origin of some mylonites by superplastic
783 flow. *Contributions to Mineralogy and Petrology, 50*(2), 93-104. doi:10.1007/BF00373329

784 Bürgmann, R., & Dresen, G. (2008). Rheology of the lower crust and upper mantle: Evidence
785 from rock mechanics, geodesy, and field observations. *Annual Review of Earth and Planetary*
786 *Sciences, 36*. doi:10.1146/annurev.earth.36.031207.124326

787 Braga, R., Massonne, H. J., & Morten, L. (2007). An early metamorphic stage for the Variscan
788 Ulten Zone gneiss (NE Italy): evidence from mineral inclusions in kyanite. *Mineralogical*
789 *Magazine, 71*(6), 691-702. doi:10.1180/minmag.2007.071.6.691

790 Braga, R., & Sapienza, G. T. (2007). The retrograde evolution of a dolomite-bearing hydrous
791 peridotite from the Ulten Zone (Italian Alps). *GeoActa, 6*, 37-45.

792 Bruijn, R. H., & Skemer, P. (2014). Grain-size sensitive rheology of orthopyroxene. *Geophysical*
793 *Research Letters, 41*(14), 4894-4903. doi:10.1002/2014GL060607

794 Bystricky, M., & Mackwell, S. (2001). Creep of dry clinopyroxene aggregates. *Journal of*
795 *Geophysical Research: Solid Earth, 106*(B7), 13443-13454. doi:10.1029/2001JB000333

796 Bystricky, M., Lawlis, J., Mackwell, S., Heidelbach, F., & Raterron, P. (2016). High-temperature
797 deformation of enstatite aggregates. *Journal of Geophysical Research: Solid Earth, 121*(9),
798 6384-6400. doi:10.1002/2016JB013011

799 Carswell, D.A. (1990). *Eclogite Facies Rocks*. Glasgow: Blackie.

800 Christensen, N. I., & Lundquist, S. M. (1982). Pyroxene orientation within the upper mantle.
801 *Geological Society of America Bulletin, 93*(4), 279-288. doi:10.1130/0016-
802 7606(1982)93<279:POWTUM>2.0.CO;2

803 Connolly, J. A. (2005). Computation of phase equilibria by linear programming: a tool for
804 geodynamic modeling and its application to subduction zone decarbonation. *Earth and Planetary*
805 *Science Letters, 236*(1-2), 524-541. doi: 10.1016/j.epsl.2005.04.033

806 Dantas, C., Ceuleneer, G., Gregoire, M., Python, M., Freydier, R., Warren, J., & Dick, H. J. B.
807 (2007). Pyroxenites from the Southwest Indian Ridge, 9–16 E: cumulates from incremental melt
808 fractions produced at the top of a cold melting regime. *Journal of Petrology, 48*(4), 647-660.
809 doi:10.1093/petrology/egl076

810 Dantas, C., Grégoire, M., Koester, E., Conceição, R. V., & Rieck Jr, N. (2009). The lherzolite–
811 websterite xenolith suite from Northern Patagonia (Argentina): evidence of mantle–melt reaction
812 processes. *Lithos, 107*(1-2), 107-120. doi:10.1016/j.lithos.2008.06.012

De Bresser, J., Ter Heege, J., & Spiers, C. (2001). Grain size reduction by dynamic recrystallization: can it result in major rheological weakening?. *International Journal of Earth Sciences, 90*(1), 28-45. doi:10.1007/s005310000149

Del Moro, A., Martin, S., & Prosser, G. (1999). Migmatites of the Ulten Zone (NE Italy), a record of melt transfer in deep crust. *Journal of Petrology*, *40*(12), 1803-1826. doi:10.1093/petroj/40.12.1803"

Demouchy, S., Schneider, S. E., Mackwell, S. J., Zimmerman, M. E., & Kohlstedt, D. L. (2009). Experimental deformation of olivine single crystals at lithospheric temperatures. *Geophysical Research Letters, 36*(4). doi:10.1029/2008GL036611

Dickey, J. S. (1970). Partial fusion products in alpine peridotites: Serrania de la Ronda and other examples. *Mineralogical Society of America Special Paper, 3*, 33-49.

Dimanov, A., & Dresen, G. (2005). Rheology of synthetic anorthite-diopside aggregates: Implications for ductile shear zones. *Journal of Geophysical Research: Solid Earth, 110*(B7). doi:10.1029/2004JB003431

Doukhan N., Doukhan J.C., Fitz Gerald J.D., Chopra P.N., Paterson M.S. (1984) A Tem Microstructural Study of Experimentally Deformed Anita Bay Dunite. In: Tressler R.E., Bradt R.C. (eds) Deformation of Ceramic Materials II. Materials Science Research, vol 18. Springer, Boston, MA. doi:10.1007/978-1-4615-6802-5_20

Doukhan, J. C., Doukhan, N., Nazé, L., & Van Duysen, J. C. (1986). Défauts de réseau et plasticité cristalline dans les pyroxènes: Une revue. *Bulletin de minéralogie, 109*(4), 377-394.

Durham, W. B., & Goetze, C. (1977). Plastic flow of oriented single crystals of olivine: 1. Mechanical data. *Journal of geophysical Research, 82*(36), 5737-5753. doi:10.1029/JB082i036p05737

Durham, W. B., Goetze, C., & Blake, B. (1977). Plastic flow of oriented single crystals of olivine: 2. Observations and interpretations of the dislocation structures. *Journal of Geophysical Research, 82*(36), 5755-5770. doi:10.1029/JB082i036p05755

Drury, M. R., Vissers, R. L., Van der Wal, D., & Strating, E. H. H. (1991). Shear localisation in upper mantle peridotites. *Pure and Applied Geophysics, 137*(4), 439-460. doi:10.1007/BF00879044

Frets, E., Tommasi, A., Garrido, C. J., Padrón-Navarta, J. A., Amri, I., & Targuisti, K. (2012). Deformation processes and rheology of pyroxenites under lithospheric mantle conditions. *Journal of Structural Geology, 39*, 138-157. doi: 10.1016/j.jsg.2012.02.019

Fumagalli, P., & Poli, S. (2005). Experimentally determined phase relations in hydrous peridotites to 6· 5 GPa and their consequences on the dynamics of subduction zones. *Journal of Petrology, 46*(3), 555-578. doi:10.1093/petrology/egh088

Furusho, M., & Kanagawa, K. (1999). Transformation-induced strain localization in a lherzolite mylonite from the Hidaka metamorphic belt of central Hokkaido, Japan. *Tectonophysics, 313*(4), 411-432. doi:10.1016/S0040-1951(99)00215-2

Garrido, C. J., & Bodinier, J. L. (1999). Diversity of mafic rocks in the Ronda peridotite: evidence for pervasive melt-rock reaction during heating of subcontinental lithosphere by upwelling asthenosphere. *Journal of petrology, 40*(5), 729-754. doi:10.1093/petroj/40.5.729

Gasparik, T. (1990). Phase relations in the transition zone. *Journal of Geophysical Research: Solid Earth, 95*(B10), 15751-15769. doi:10.1029/JB095iB10p15751

Gebauer D., & Grünenfelder, M. (1978). U-Pb dating of alpine-type garnet-peridotites example: Val Ultimo (Eastern Alps, northern Italy). U. S. Geol. Surv. Open-File Report, OF 78-0701: 135-137

Godard, G., Martin, S., & Prosser, G. (1996). Variscan migmatites, eclogites and garnet-peridotites of the Ulten zone, Eastern Austroalpine system. *Tectonophysics, 259*(4), 313-341. doi:10.1016/0040-1951(95)00145-X

Godard, G., & van Roermund, H. L. (1995). Deformation-induced clinopyroxene fabrics from eclogites. Journal of Structural Geology, 17(10), 1425-1443. doi:10.1016/0191-8141(95)00038-F

Gysi, A. P., Jagoutz, O., Schmidt, M. W., & Targuisti, K. (2011). Petrogenesis of pyroxenites and melt infiltrations in the ultramafic complex of Beni Bousera, Northern Morocco. *Journal of Petrology, 52*(9), 1679-1735. doi:10.1093/petrology/egr026

Handy, M. R. (1989). Deformation regimes and the rheological evolution of fault zones in the lithosphere: the effects of pressure, temperature, grainsize and time. *Tectonophysics, 163*(1-2), 119-152. doi:10.1016/0040-1951(89)90122-4

Handy, M. R. (1990). The solid-state flow of polymineralic rocks. *Journal of Geophysical Research: Solid Earth, 95*(B6), 8647-8661. doi:10.1029/JB095iB06p08647

Hansen, L. N., Zimmerman, M. E., & Kohlstedt, D. L. (2011). Grain boundary sliding in San Carlos olivine: Flow law parameters and crystallographic-preferred orientation. *Journal of Geophysical Research: Solid Earth, 116*(B8). doi:10.1029/2011JB008220

Hauzenberger, C. A., Höller, W., & Hoinkes, G. (1996). Transition from eclogite to amphibolite-facies metamorphism in the Austroalpine Ulten Zone. *Mineralogy and Petrology, 58*(3-4), 111-130. doi:10.1007/BF01172092

Hermann, J., & Green, D. H. (2001). Experimental constraints on high pressure melting in subducted crust. *Earth and Planetary Science Letters, 188*(1-2), 149-168. doi:10.1016/S0012-821X(01)00321-1

881 Herzberg, C., Riccio, L., Chiesa, S., Fornoni, A., Gatto, G. O., Gregnanin, A., Piccirillo, E. M. &
882 Scolari, A. (1977). Petrogenetic evolution of the spinel–garnet-lherzolite in the Austridic
883 crystalline basement from Val Clapa (Alto Adige, northeastern Italy). *Memorie dell'Istituto di*
884 *Geologia, Universita` di Padova 30*, 3-28.

885 Hidas, K., Garrido, C. J., Tommasi, A., Padrón-Navarta, J. A., Thielmann, M., Konc, Z., &
886 Marchesi, C. (2013). Strain localization in pyroxenite by reaction-enhanced softening in the
887 shallow subcontinental lithospheric mantle. *Journal of Petrology, 54*(10), 1997-2031.
888 doi:10.1093/petrology/egt039

889 Hielscher, R., & Schaeben, H. (2008). A novel pole figure inversion method: specification of the
890 MTEX algorithm. *Journal of Applied Crystallography, 41*(6), 1024-1037.
891 doi:10.1107/S0021889808030112

892 Hirth, G., & Kohlstedf, D. (2003). Rheology of the upper mantle and the mantle wedge: A view
893 from the experimentalists. *Geophysical Monograph-American Geophysical Union, 138*, 83-106.
894 doi:10.1029/138GM06

895 Hoinkes, G., & Thöni, M. (1993). Evolution of the Ötztal-Stubai, Scarl-Campo and Ulten
896 basement units. In von Raumer J.F., Neubauer F. (Eds.), *Pre-mesozoic geology in the Alps* (pp.
897 485-494). Berlin, Heidelberg: Springer. doi: 10.1007/978-3-642-84640-3

898 Holland, T. J. B., & Powell, R. T. J. B. (1998). An internally consistent thermodynamic data set
899 for phases of petrological interest. *Journal of metamorphic Geology, 16*(3), 309-343. doi:
900 10.1111/j.1525-1314.1998.00140.x

901 Honda, S. (1985). Thermal structure beneath Tohoku, northeast Japan. *Tectonophysics, 112*(1-4),
902 69-102. doi:10.1016/0040-1951(85)90173-8

903 Irving, A. J. (1974). Geochemical and high pressure experimental studies of garnet pyroxenite
904 and pyroxene granulite xenoliths from the Delegate basaltic pipes, Australia. *Journal of*
905 *Petrology, 15*(1), 1-40. doi:10.1093/petrology/15.1.1

906 Ishii, K., & Sawaguchi, T. (2002). Lattice-and shape-preferred orientation of orthopyroxene
907 porphyroclasts in peridotites: an application of two-dimensional numerical modeling. *Journal of*
908 *Structural Geology, 24*(3), 517-530. doi:10.1016/S0191-8141(01)00078-5

909 Jahn, S., & Martoňák, R. (2008). Plastic deformation of orthoenstatite and the ortho-to high-
910 pressure clinoenstatite transition: A metadynamics simulation study. *Physics and Chemistry of*
911 *Minerals, 35*(1), 17-23. doi:10.1007/s00269-007-0194-2

912 Jaroslow, G. E., Hirth, G., & Dick, H. J. B. (1996). Abyssal peridotite mylonites: implications
913 for grain-size sensitive flow and strain localization in the oceanic lithosphere. *Tectonophysics,*
914 *256*(1-4), 17-37. doi:10.1016/0040-1951(95)00163-8

915 Jung, H., Katayama, I., Jiang, Z., Hiraga, T., & Karato, S. I. (2006). Effect of water and stress on
916 the lattice-preferred orientation of olivine. *Tectonophysics, 421*(1-2), 1-22.
917 doi:10.1016/j.tecto.2006.02.011

918 Jung, H., Park, M., Jung, S., & Lee, J. (2010). Lattice preferred orientation, water content, and
919 seismic anisotropy of orthopyroxene. *Journal of Earth Science, 21*(5), 555-568.
920 doi:10.1007/s12583-010-0118-9

921 Kaczmarek, M. A., & Tommasi, A. (2011). Anatomy of an extensional shear zone in the mantle,
922 Lanzo massif, Italy. *Geochemistry, Geophysics, Geosystems, 12*(8). doi:10.1029/2011GC003627

923 Kempton, P. D., & Stephens, C. J. (1997). Petrology and geochemistry of nodular websterite
924 inclusions in harzburgite, Hole 920D. In J.A. Karson, M. Cannat, D.J. Miller, D. Elthon (Eds.),
925 Proceedings of the Ocean Drilling Program, Scientific Results (Vol. 153, pp. 321-331). College
926 Station, TX: Texas A&M University Digital Library. doi:10.2973/odp.proc.sr.153.030.1997

927 Keshav, S., Sen, G., & Presnall, D. C. (2007). Garnet-bearing xenoliths from Salt Lake Crater,
928 Oahu, Hawaii: High-pressure fractional crystallization in the oceanic mantle. *Journal of*
929 *Petrology, 48*(9), 1681-1724. doi:10.1093/petrology/egm035

930 Kornprobst, J. (1969). Le massif ultrabasique des Beni Bouchera (Rif Interne, Maroc): Etude des
931 péridotites de haute température et de haute pression, et des pyroxénolites, à grenat ou sans
932 grenat, qui leur sont associées. *Contributions to Mineralogy and Petrology, 23*(4), 283-322.
933 doi:10.1007/BF00371425

934 Kornprobst, J. (1970). Les péridotites et les pyroxénolites du massif ultrabasique des Beni
935 Bouchera: une étude expérimentale entre 1100 et 1550° C, sous 15 à 30 kilobars de pression
936 sèche. *Contributions to Mineralogy and Petrology, 29*(4), 290-309. doi:10.1007/BF00371277

937 Kornprobst, J., Piboule, M., Roden, M., & Tabit, A. (1990). Corundum-bearing garnet
938 clinopyroxenites at Beni Bousera (Morocco): original plagioclase-rich gabbros recrystallized at
939 depth within the mantle?. *Journal of Petrology, 31*(3), 717-745. doi:10.1093/petrology/31.3.717

940 Lavina, B., Carbonin, S., Russo, U., & Tumiati, S. (2006). The crystal structure of dissakisite-
941 (La) and structural variations after annealing of radiation damage. *American Mineralogist, 91*(1),
942 104-110. doi:10.2138/am.2006.1721

943 Linckens, J., Bruijn, R. H., & Skemer, P. (2014). Dynamic recrystallization and phase mixing in
944 experimentally deformed peridotite. *Earth and Planetary Science Letters, 388*, 134-142.
945 doi:10.1016/j.epsl.2013.11.037

946 Mainprice, D., Barruol, G., Ismail, W. B., (2000). The Seismic Anisotropy of the Earth's Mantle
947 from Single Crystal to Polycrystal. *Geophysical Monograph, 117*, 237–264.
948 doi:10.1029/GM117p0237

949 Malaspina, N., Hermann, J., Scambelluri, M., & Compagnoni, R. (2006). Polyphase inclusions in
950 garnet–orthopyroxenite (Dabie Shan, China) as monitors for metasomatism and fluid-related
951 trace element transfer in subduction zone peridotite. *Earth and Planetary Science Letters, 249*(3-
952 4), 173-187. doi:10.1016/j.epsl.2006.07.017

953 Malaspina, N., & Tumiati, S. (2012). The role of COH and oxygen fugacity in subduction-zone
954 garnet peridotites. *European Journal of Mineralogy, 24*(4), 607-618. doi:10.1127/0935-
955 1221/2012/0024-2213

956 Marocchi, M., Hermann, J., Tropper, P., Bargossi, G. M., & Mair, V. (2010). Amphibole and
957 phlogopite in "hybrid" metasomatic bands monitor trace element transfer at the interface
958 between felsic and ultramafic rocks (Eastern Alps, Italy). *Lithos, 117*(1-4), 135-148.
959 doi:10.1016/j.lithos.2010.02.011

960 Marocchi, M., Mair, V., Tropper, P., & Bargossi, G. M. (2009). Metasomatic reaction bands at
961 the Mt. Hochwart gneiss-peridotite contact (Ulten Zone, Italy): insights into fluid-rock
962 interaction in subduction zones. *Mineralogy and Petrology, 95*(3-4), 251. doi:10.1007/s00710-
963 009-0043-8

964 Martin, S., Godard, G., Prosser, G., Schiavo, A., Bernoulli, D., & Ranalli, G. (1998). Evolution
965 of the deep crust at the junction Austroalpine/Southalpine: the Tonale Nappe. *Memorie di*
966 *Scienze Geologiche 50*, 3-50.

967 Martin, S., Morten, L. & Prosser, G. (1993). Metamorphic and structural evolution of the Spl- to
968 Grt-peridotites and surrounding basement rocks from the Nonsberg area. In Morten, L. (Eds)
969 *Italian Eclogites and Related Rocks* (Vol. 13, pp. 237-251). Roma: Accademia Nazionale delle
970 Scienze detta dei XL.

971 Miranda, E. A., Hirth, G., & John, B. E. (2016). Microstructural evidence for the transition from
972 dislocation creep to dislocation-accommodated grain boundary sliding in naturally deformed
973 plagioclase. *Journal of Structural Geology, 92*, 30-45. doi:10.1016/j.jsg.2016.09.002

974 Morishita, T., & Arai, S. (2001). Petrogenesis of corundum-bearing mafic rock in the Horoman
975 Peridotite Complex, Japan. *Journal of Petrology, 42*(7), 1279-1299.
976 doi:10.1093/petrology/42.7.1279

977 Morishita, T., Arai, S., Gervilla, F., & Green, D. H. (2003). Closed-system geochemical
978 recycling of crustal materials in alpine-type peridotite. *Geochimica et Cosmochimica Acta, 67*(2),
979 303-310. doi:10.1016/S0016-7037(02)01079-7

980 Morten, L., & Obata, M. (1983). Possible high-temperature origin of pyroxenite lenses within
981 garnet peridotite, northern Italy. *Bulletin de minéralogie, 106*(6), 775-780.

982 Morten, L. & Trommsdorff, V. (2003). Metamorphism and textures of dry and hydrous garnet
983 peridotites. In Carswell, D.A. & Compagnoni, R. (Eds.), *Ultrahigh Pressure Metamorphism,*
984 *EMU Notes in Mineral*ogy (vol. 5 pp. 443-46). Budapest: Eotvos University Press.

985 Mukasa, S. B., & Shervais, J. W. (1999). Growth of subcontinental lithosphere: evidence from
986 repeated dike injections in the Balmuccia lherzolite massif, Italian Alps. *Lithos, 48*(1-4), 287-
987 316. doi:10.1016/S0024-4937(99)00033-X

988 Maruyama, G., & Hiraga, T. (2017). Grain-to multiple-grain-scale deformation processes during
989 diffusion creep of forsterite + diopside aggregate: 1. Direct observations. *Journal of Geophysical*
990 *Research: Solid Earth, 122*(8), 5890-5915. doi:10.1002/2017JB014254

991 Nazé, L., Doukhan, N., Doukhan, J. C., & Latrous, K. (1987). A TEM study of lattice defects in
992 naturally and experimentally deformed orthopyroxenes. *Bulletin de minéralogie, 110*(5), 497-
993 512. doi:10.3406/bulmi.1987.7993

994 Newman, J., Lamb, W. M., Drury, M. R., & Vissers, R. L. (1999). Deformation processes in a
995 peridotite shear zone: reaction-softening by an H_2O-deficient, continuous net transfer reaction.
996 *Tectonophysics, 303*(1-4), 193-222. doi:10.1016/S0040-1951(98)00259-5

997 Nimis, P., & Morten, L. (2000). P-T evolution of 'crustal' garnet peridotites and included
998 pyroxenites from Nonsberg area (upper Austroalpine), NE Italy: from the wedge to the slab.
999 *Journal of Geodynamics, 30*(1-2), 93-115. doi:10.1016/S0264-3707(99)00029-0

1000 Obata, M., & Morten, L. (1987). Transformation of spinel lherzolite to garnet lherzolite in
1001 ultramafic lenses of the Austridic crystalline complex, northern Italy. *Journal of Petrology,*
1002 *28*(3), 599-623. doi:10.1093/petrology/28.3.599

1003 Pellegrino, L., Malaspina, N., Zanchetta, S., Langone, A., & Tumiati, S. (2020). High pressure
1004 melting of eclogites and metasomatism of garnet peridotites from Monte Duria Area (Central
1005 Alps, N Italy): A proxy for melt-rock reaction during subduction. *Lithos, 358-359*, 105391.
1006 doi:10.1016/j.lithos.2020.105391

1007 Précigout, J., Gueydan, F., Gapais, D., Garrido, C. J., & Essaifi, A. (2007). Strain localisation in
1008 the subcontinental mantle—a ductile alternative to the brittle mantle. Tectonophysics, 445(3-4),
1009 318-336. doi:10.1016/j.tecto.2007.09.002

1010 Prior, D. J., Wheeler, J., Peruzzo, L., Spiess, R., & Storey, C. (2002). Some garnet
1011 microstructures: an illustration of the potential of orientation maps and misorientation analysis in
1012 microstructural studies. *Journal of Structural Geology, 24*(6-7), 999-1011. doi:10.1016/S0191-
1013 8141(01)00087-6

1014 Raleigh, C. B., Kirby, S. H., Carter, N. L., & Lallemant, H. A. (1971). Slip and the clinoenstatite
1015 transformation as competing rate processes in enstatite. *Journal of Geophysical Research,*
1016 *76*(17), 4011-4022. doi:10.1029/JB076i017p04011

1017 Rampone, E., & Morten, L. (2001). Records of crustal metasomatism in the garnet peridotites of
1018 the Ulten Zone (Upper Austroalpine, Eastern Alps). *Journal of Petrology, 42*(1), 207-219.
1019 doi:10.1093/petrology/42.1.207

1020 Rampone, E., & Borghini, G. (2008). Melt migration and intrusion in the Erro-Tobbio peridotites
1021 (Ligurian Alps, Italy): Insights on magmatic processes in extending lithospheric mantle.
1022 *European Journal of Mineralogy, 20*(4), 573-585. doi:10.1127/0935-1221/2008/0020-1807

1023 Ranalli, G., Martin, S., & Mahatsente, R. (2005). Continental subduction and exhumation: an
1024 example from the Ulten Unit, Tonale Nappe, Eastern Austroalpine. *Geological Society, London,*
1025 *Special Publications, 243*(1), 159-174. doi:10.1144/GSL.SP.2005.243.01.1

1026 Raterron, P., Detrez, F., Castelnau, O., Bollinger, C., Cordier, P., & Merkel, S. (2014).
1027 Multiscale modeling of upper mantle plasticity: From single-crystal rheology to multiphase
1028 aggregate deformation. *Physics of the Earth and Planetary Interiors, 228*, 232-243.
1029 doi:10.1016/j.pepi.2013.11.012

1030 Rivalenti, G., Mazzucchelli, M., Vannucci, R., Hofmann, A. W., Ottolini, L., Bottazzi, P., &
1031 Obermiller, W. (1995). The relationship between websterite and peridotite in the Balmuccia
1032 peridotite massif (NW Italy) as revealed by trace element variations in clinopyroxene.
1033 *Contributions to Mineralogy and Petrology, 121*(3), 275-288. doi:10.1007/BF02688243

1034 Rutter, E. H., & Brodie, K. H. (1988). The role of tectonic grain size reduction in the rheological
1035 stratification of the lithosphere. *Geologische Rundschau, 77*(1), 295-307.
1036 doi:10.1007/BF01848691

1037 Sapienza, G. T., Scambelluri, M., & Braga, R. (2009). Dolomite-bearing orogenic garnet
1038 peridotites witness fluid-mediated carbon recycling in a mantle wedge (Ulten Zone, Eastern
1039 Alps, Italy). *Contributions to Mineralogy and Petrology*, *158*(3), 401-420. doi:10.1007/s00410-
1040 009-0389-2

1041 Sawyer, E. W. (Ed.). (2008). *Atlas of migmatites: The Canadian Mineralogist Special*
1042 *Publication 9*. Ottawa: NRC Research press.

1043 Scambelluri, M., Hermann, J., Morten, L., & Rampone, E. (2006). Melt-versus fluid-induced
1044 metasomatism in spinel to garnet wedge peridotites (Ulten Zone, Eastern Italian Alps): clues
1045 from trace element and Li abundances. *Contributions to Mineralogy and Petrology, 151*(4), 372.
1046 doi:10.1007/s00410-006-0064-9

1047 Scambelluri, M., Rampone, E., Braga, R., & Malaspina, N. (2010). The Variscan garnet
1048 peridotites from the Eastern Alps (Ulten Zone): Records of subduction metasomatism in the
1049 mantle wedge. *Journal of the Virtual Explorer*. In: Marco Beltrando, Angelo Peccerillo,
1050 Massimo Mattei, Sandro Conticelli, and Carlo Doglioni (Eds.), The Geology of Italy (Vol. 36,
1051 paper 28). doi:10.3809/jvirtex.2009.00259

1052 Schmädicke, E. (2000). Phase relations in peridotitic and pyroxenitic rocks in the model systems
1053 CMASH and NCMASH. *Journal of Petrology, 41*(1), 69-86. doi:10.1093/petrology/41.1.69

1054 Skemer, P., Katayama, I., & Karato, S. I. (2006). Deformation fabrics of the Cima di Gagnone
1055 peridotite massif, Central Alps, Switzerland: evidence of deformation at low temperatures in the

presence of water. *Contributions to Mineralogy and Petrology, 152*(1), 43. doi:10.1007/s00410-006-0093-4

Skemer, P., Warren, J. M., Kelemen, P. B., & Hirth, G. (2010). Microstructural and rheological evolution of a mantle shear zone. *Journal of Petrology, 51*(1-2), 43-53. doi:10.1093/petrology/egp057

Skrotzki, W. (1994). Defect structure and deformation mechanisms in naturally deformed augite and enstatite. *Tectonophysics, 229*(1-2), 43-68. doi:10.1016/0040-1951(94)90005-1

Skrotzki, W., Wedel, A., Weber, K., & Müller, W. F. (1990). Microstructure and texture in lherzolites of the Balmuccia massif and their significance regarding the thermomechanical history. *Tectonophysics, 179*(3-4), 227-251. doi:10.1016/0040-1951(90)90292-G

Soustelle, V., Tommasi, A., Demouchy, S., & Ionov, D. A. (2010). Deformation and fluid–rock interaction in the supra-subduction mantle: microstructures and water contents in peridotite xenoliths from the Avacha Volcano, Kamchatka. *Journal of Petrology, 51*(1-2), 363-394. doi:10.1093/petrology/egp085

Spengler, D., Obata, M., Hirajima, T., Ottolini, L., Ohfuji, H., Tamura, A., & Arai, S. (2012). Exsolution of garnet and clinopyroxene from high-Al pyroxenes in Xugou peridotite, Eastern China. *Journal of Petrology, 53*(7), 1477-1504. doi:10.1093/petrology/egs023

Susini, S., & Martin, S. (1996). Microstrutture nelle peridotiti della serie d'Ultimo (Austroalpino superiore, Alpi orientali). *Atti Ticinesi di Scienze della Terra, 4,* 47-63.

Svahnberg, H., & Piazolo, S. (2010). The initiation of strain localisation in plagioclase-rich rocks: Insights from detailed microstructural analyses. *Journal of Structural Geology, 32*(10), 1404-1416. doi:10.1016/j.jsg.2010.06.011

Takazawa, E., Frey, F. A., Shimizu, N., Saal, A., & Obata, M. (1999). Polybaric petrogenesis of mafic layers in the Horoman peridotite complex, Japan. *Journal of Petrology, 40*(12), 1827-1851. doi:10.1093/petroj/40.12.1827

Tikoff, B., Larson, C. E., Newman, J., & Little, T. (2010). Field-based constraints on finite strain and rheology of the lithospheric mantle, Twin Sisters, Washington. *Lithosphere, 2*(6), 418-422. doi:10.1130/L97.1

Tommasi, A., Vauchez, A., & Ionov, D. A. (2008). Deformation, static recrystallization, and reactive melt transport in shallow subcontinental mantle xenoliths (Tok Cenozoic volcanic field, SE Siberia). Earth and Planetary Science Letters, 272(1-2), 65-77. doi:10.1016/j.epsl.2008.04.020

Tommasi, A., & Vauchez, A. (2015). Heterogeneity and anisotropy in the lithospheric mantle. *Tectonophysics, 661*, 11-37. doi:10.1016/j.tecto.2015.07.026

Toy, V. G., Newman, J., Lamb, W., & Tikoff, B. (2010). The role of pyroxenites in formation of shear instabilities in the mantle: evidence from an ultramafic ultramylonite, Twin Sisters Massif, Washington. *Journal of Petrology, 51*(1-2), 55-80. doi:10.1093/petrology/egp059

Treagus, S. H., & Sokoutis, D. (1992). Laboratory modelling of strain variation across rheological boundaries. *Journal of Structural Geology, 14*(4), 405-424. doi:10.1016/0191-8141(92)90102-3

Tumiati, S., Godard, G., Martin, S., Klötzli, U., & Monticelli, D. (2007). Fluid-controlled crustal metasomatism within a high-pressure subducted mélange (Mt. Hochwart, Eastern Italian Alps). *Lithos, 94*(1-4), 148-167. doi:10.1016/j.lithos.2006.06.009

Tumiati, S., Godard, G., Martin, S., Nimis, P., Mair, V., & Boyer, B. (2005). Dissakisite-(La) from the Ulten zone peridotite (Italian Eastern Alps): A new end-member of the epidote group. *American Mineralogist, 90*(7), 1177-1185. doi:10.2138/am.2005.1710

Tumiati, S., & Martin, S. (2003). Garnet-peridotite in the Italian Eastern Alps: 150 years of discoveries. *Memorie di Scienze Geologiche dell'Università di Padova, 55*, 31-46.

Tumiati, S., Thöni, M., Nimis, P., Martin, S., & Mair, V. (2003). Mantle-crust interactions during Variscan subduction in the Eastern Alps (Nonsberg–Ulten zone): geochronology and new petrological constraints. *Earth and Planetary Science Letters, 210*(3-4), 509-526. doi:10.1016/S0012-821X(03)00161-4

Tumiati, S., Zanchetta, S., Pellegrino, L., Ferrario, C., Casartelli, S., & Malaspina, N. (2018). Granulite-facies overprint in garnet peridotites and kyanite eclogites of Monte Duria (Central Alps, Italy): clues from srilankite-and sapphirine-bearing symplectites. *Journal of Petrology, 59*(1), 115-151. doi:10.1093/petrology/egy021

Ulrich, S., & Mainprice, D. (2005). Does cation ordering in omphacite influence development of lattice-preferred orientation?. *Journal of Structural Geology, 27*(3), 419-431. doi:10.1016/j.jsg.2004.11.003

Van Acken, D., Becker, H., Walker, R. J., McDonough, W. F., Wombacher, F., Ash, R. D., & Piccoli, P. M. (2010). Formation of pyroxenite layers in the Totalp ultramafic massif (Swiss Alps)–insights from highly siderophile elements and Os isotopes. *Geochimica et Cosmochimica Acta, 74*(2), 661-683. doi:10.1016/j.gca.2009.10.007

Van Duysen, J. C., & Doukhan, J. C. (1984). Room temperature microplasticity of a spodumene $LiAlSi_2O_6$. *Physics and Chemistry of Minerals, 10*(3), 125-132. doi:10.1007/BF00309647

Van Duysen, J. C., Doukhan, N., & Doukhan, J. C. (1985). Transmission electron microscope study of dislocations in orthopyroxene $(Mg, Fe)_2Si_2O_6$. *Physics and Chemistry of Minerals, 12*(1), 39-44. doi:10.1007/BF00348745

Vannucci, R., Shimizu, N., Piccardo, G. B., Ottolini, L., & Bottazzi, P. (1993). Distribution of trace elements during breakdown of mantle garnet: an example from Zabargad. *Contributions to Mineralogy and Petrology, 113*(4), 437-449. doi:10.1007/BF00698314

Vauchez, A., & Garrido, C. J. (2001). Seismic properties of an asthenospherized lithospheric mantle: constraints from lattice preferred orientations in peridotite from the Ronda massif. *Earth and Planetary Science Letters, 192*(2), 235-249. doi:10.1016/S0012-821X(01)00448-4

Vauchez, A., Tommasi, A., & Mainprice, D. (2012). Faults (shear zones) in the Earth's mantle. *Tectonophysics, 558*, 1-27. doi:10.1016/j.tecto.2012.06.006

Wang, J., Hattori, K. H., & Stern, C. R. (2008). Metasomatic origin of garnet orthopyroxenites in the subcontinental lithospheric mantle underlying Pali Aike volcanic field, southern South America. *Mineralogy and Petrology, 94*(3-4), 243. doi:10.1007/s00710-008-0017-2

Warren, J. M., & Hirth, G. (2006). Grain size sensitive deformation mechanisms in naturally deformed peridotites. Earth and Planetary Science Letters, 248(1-2), 438-450. doi:10.1016/j.epsl.2006.06.006

Warren, J. M., Shimizu, N., Sakaguchi, C., Dick, H. J. B., & Nakamura, E. (2009). An assessment of upper mantle heterogeneity based on abyssal peridotite isotopic compositions. *Journal of Geophysical Research: Solid Earth, 114*(B12). doi:10.1029/2008JB006186

Wheeler, J., Prior, D., Jiang, Z., Spiess, R., & Trimby, P. (2001). The petrological significance of misorientations between grains. *Contributions to mineralogy and petrology, 141*(1), 109-124. doi:10.1007/s004100000225

White, S. (1977). Geological significance of recovery and recrystallization processes in quartz. *Tectonophysics, 39*(1-3), 143-170. doi:10.1016/0040-1951(77)90093-2

White, S. (1979). Grain and sub-grain size variations across a mylonite zone. *Contributions to Mineralogy and Petrology, 70*(2), 193-202. doi:10.1007/BF00374448

White, S. H., Burrows, S. E., Carreras, J., Shaw, N. D., & Humphreys, F. J. (1980). On mylonites in ductile shear zones. *Journal of Structural Geology, 2*(1-2), 175-187. doi:10.1016/0191-8141(80)90048-6

Xu, Z., Wang, Q., Ji, S., Chen, J., Zeng, L., Yang, J., & Wenk, H. R. (2006). Petrofabrics and seismic properties of garnet peridotite from the UHP Sulu terrane (China): implications for olivine deformation mechanism in a cold and dry subducting continental slab. *Tectonophysics, 421*(1-2), 111-127. doi:10.1016/j.tecto.2006.04.010

Yu, S. Y., Xu, Y. G., Ma, J. L., Zheng, Y. F., Kuang, Y. S., Hong, L. B., ... & Tong, L. X. (2010). Remnants of oceanic lower crust in the subcontinental lithospheric mantle: trace element and Sr–Nd–O isotope evidence from aluminous garnet pyroxenite xenoliths from Jiaohe,

1158 Northeast China. *Earth and Planetary Science Letters, 297*(3-4), 413-422.
1159 doi:10.1016/j.epsl.2010.06.043

1160 Zhang, J., Green II, H. W., & Bozhilov, K. N. (2006). Rheology of omphacite at high
1161 temperature and pressure and significance of its lattice preferred orientations. *Earth and*
1162 *Planetary Science Letters, 246*(3-4), 432-443. doi:10.1016/j.epsl.2006.04.006

1163 Ziberna, L., Klemme, S., & Nimis, P. (2013). Garnet and spinel in fertile and depleted mantle:
1164 insights from thermodynamic modelling. *Contributions to Mineralogy and Petrology, 166*(2),
1165 411-421. doi:10.1007/s00410-013-0882-5
1166